Electronic Supporting Information

Amorphous Tetrazine-Triazine-Functionalized Covalent Organic Framework for Adsorption and Removal of Dyes

Shubham Kumar, Kusum Kumari, Saurabh K. Singh, Bharat Z. Dholakiya and Ritambhara Jangir*

Table of Contents

Schemes and Figures

other adsorbents, (b) Comparison of the adsorption capacity and Bet Surface area of TzTPT-COF with different type of other adsorbents.

S1. Materials

4-hydroxybenzaldehyde, triethylamine, 1,4-Dioxane, cyanuric chloride, ethyl acetate, 4-aminobenzonitrile, hydrazine hydrate, DMSO and hydrogen peroxide were purchased from Sigma Aldrich. Sulphur powder, ethanol, acetone were received from Spectrochem. All the reagents and solvents were of analytical grade, hence were used without any further purification.

S2. Characterization

^{1}H and ^{13}C NMR spectroscopy. NMR spectra were recorded using an ECS 400MHz (JEOL) NMR spectrometer, using DMSO-d_6 and $CDCl_3$ as solvents and tetramethylsilane (TMS) as the external standard. Chemical shifts are provided in parts per million (ppm).

Fourier transform infrared (FT-IR) spectroscopy. FT-IR spectra were recorded using a SHIMADZU IR Affinity-1 Instrument; 45 scans were collected at a resolution of 4 cm^{-1}.

^{13}C Solid-State Nuclear Magnetic Resonance (NMR) Spectroscopy. Solid-State Nuclear Magnetic Resonance spectrum was recorded at IISC Bangalore using JEOL 400MHz (ECX400) spectrometer solid state NMR spectrometer and a Bruker magic-angle-spinning (MAS) probe, running 32,000 scans.

Powder X-ray diffraction. Powder XRDs were carried out using a X-Ray Diffractometer (Panalytical X Pert Pro) instruments. The data analysis was performed using the Reflex module of the Materials Studio V6.0.

Thermo-gravimetric analysis. Thermo-gravimetric analysis was carried out on Thermogravimetric Differential thermal analyzer (TGA-DTA) TA Module Q 600 system. The TGAs were done under N_2 gas flow (20ml/min) (purge + protective) and samples were heated from RT to 800 ^{o}C at 10K/min.

Surface area and porosimetry (ASAP/BET). The BET surface areas and porosimetry measurements of the prepared samples (ca. 20-100 mg) were performed using a Nova Touch LX2 gas sorption analyzer from Quantachrome surface area and porosity analyzer. Nitrogen isotherms were generated through incremental exposure to ultrahigh-purity N_2 (up to ca. 1 atm) in a liquid N_2 (77 K) bath.

Field Emission-Scanning Electron Microscopy (FE-SEM): FE-SEM was conducted using a Nova Nano FE-SEM 450 (FEI) scanning electron microscope. Samples were subjected to Pt sputtering for 100 s prior to observation.

High resolution Transmission Electron Microscopy (HR-TEM): Transmission electron microscopy (TEM) was performed using Tecnai G2 20 S-TWIN [FEI] TEM microscope operating at an accelerating voltage of (200 kV). The diffractograms were recorded at a scanning rate of 1° min^{-1} between 20° and 80°.

S3. Synthetic Procedures

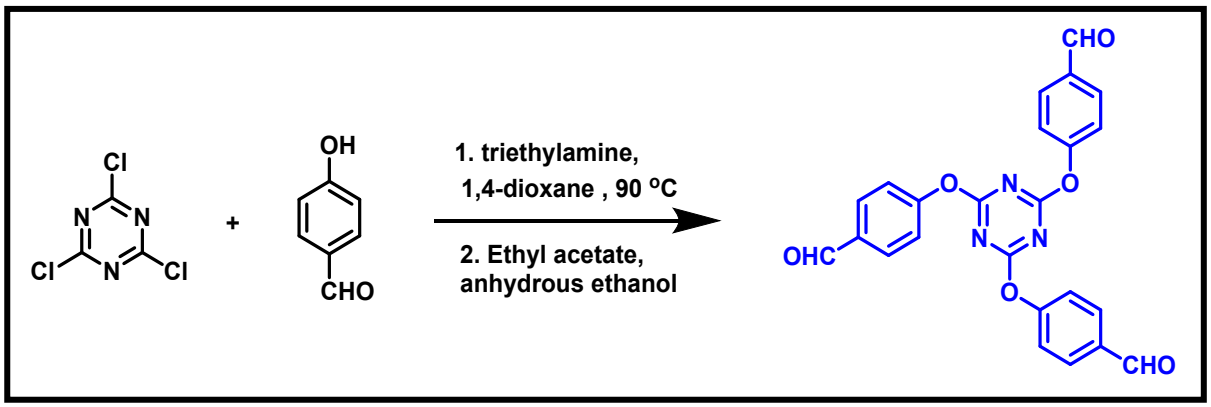

Scheme S1. Synthesis of 4,4',4''-((1,3,5-triazine-2,4,6-triyl)tris(oxy))tribenzaldehyde (TPT-CHO).

4,4',4''-((1,3,5-triazine-2,4,6-triyl)tris(oxy))tribenzaldehyde (TPT-CHO): 4,4',4''-((1,3,5-triazine-2,4,6-triyl)tris(oxy))tribenzaldehyde (TPT-CHO) was synthesized using a reported procedure.[1] A 150 mL three-necked flask was charged with 4-hydroxybenzaldehyde (6.1 g, 0.05 mol) and triethylamine (6.325 g, 0.0625 mol), dissolved in 1,4-dioxane (60 mL) as a solvent with stirring. Cyanuric chloride (2.3 g, 0.125 mol) was dissolved in 1,4-dioxane (30 mL), and the solution was slowly added dropwise to the flask and continuously stirred for 12 hours. The mixture was then heated to 90°C for 6 hours, cooled to room temperature, and the resulting white solid was filtered from the reaction mixture. The filtrate was evaporated under reduced pressure and recrystallized from a mixture of ethyl acetate and anhydrous ethanol. This resulted in a white precipitate, which was filtered, dried, and obtained as 4.8 g of the final product with a yield of 85%. The product was characterised by IR (Figure S1) and ^{1}H (Figure S2) and ^{13}C NMR (Figure S3) studies.^{1}H-NMR (DMSO-d_6, 400 MHz): δ= 9.93 (s, 3H), 7.92 (d, 6H), 7.42 (d, 6H). ^{13}C-NMR (DMSO-d6, 400 MHz):192.45, 173.21, 156.12, 134.58, 131.67, 122.86 ppm.

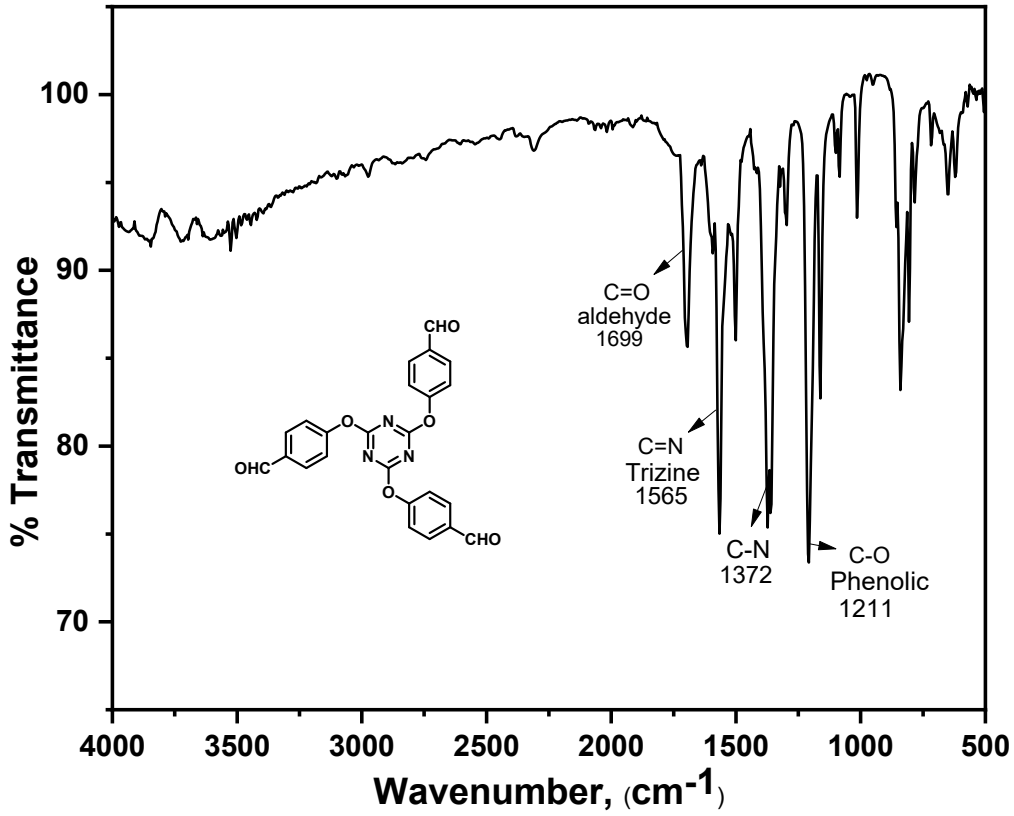

Figure S1. Fourier transform infrared spectrum of TPT-CHO.

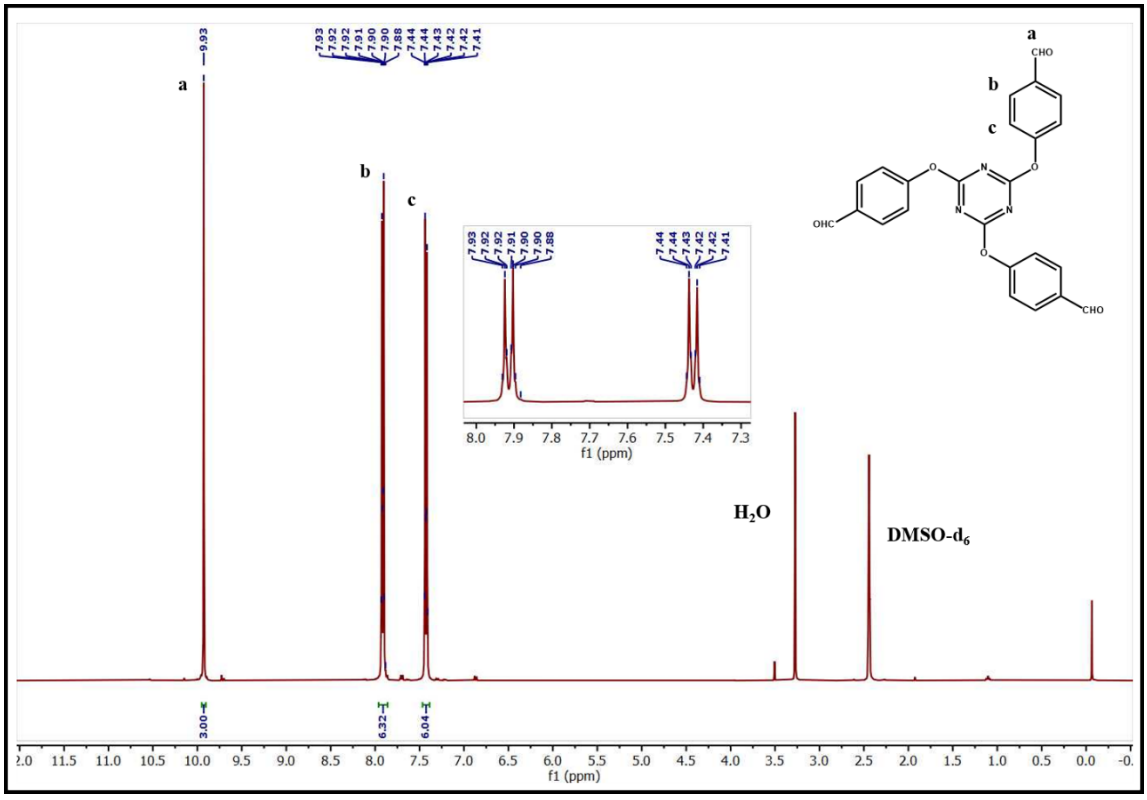

Figure S2. ^{1}H NMR spectrum of TPT-CHO in DMSO-d_6 (400 MHz).

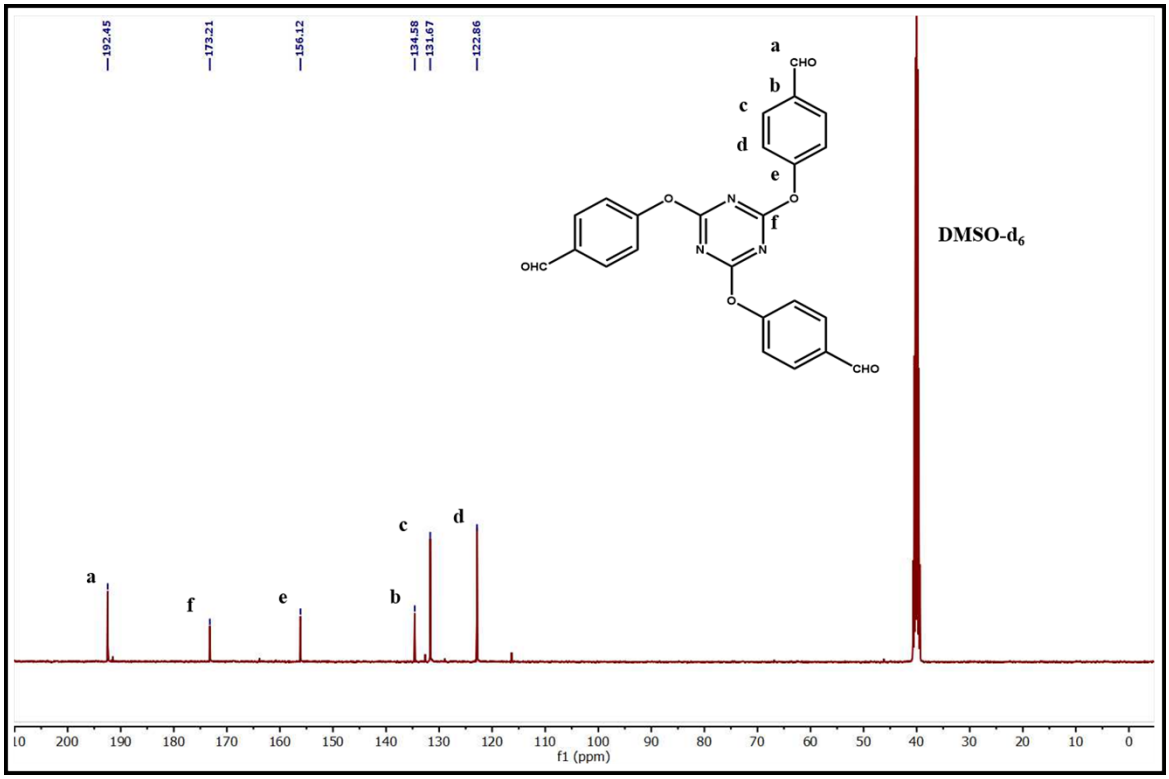

Figure S3. ^{13}C NMR spectrum of TPT-CHO in DMSO-d_6 (400 MHz).

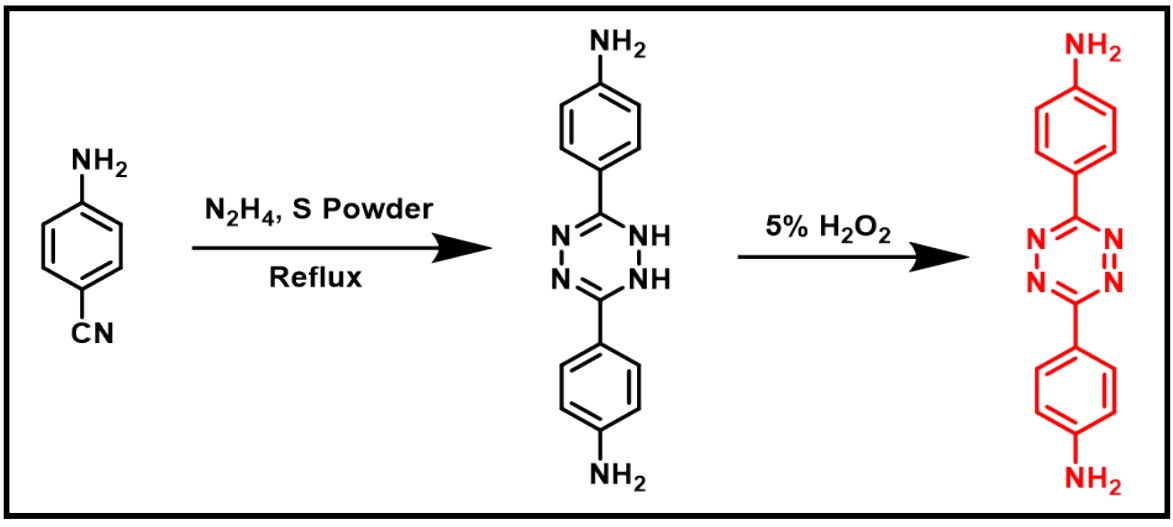

Scheme S2. Synthesis of s-tetrazine diamine (Tz).

Synthesis of s-tetrazine diamine (Tz): s-tetrazine diamine (Tz) was synthesized by the modification in the reported literature. In a typical synthesis, 4 g of 4-aminobenzonitrile was dissolved in 20 mL of methanol.[2] 15 mL of hydrazine hydrate (conc. 99%) and 4 g of sulphur powder were added to the solution, which was then refluxed at 90°C for 8 hours, leading to the formation of a bright golden yellow colored thick suspension. The suspension was filtered, washed repeatedly with methanol and acetone, and subjected to vacuum drying overnight. The resulting bright yellow powder was dispersed in dry dimethyl sulfoxide

(DMSO) by stirring and underwent an overnight oxygen (O_2) purging process. A bright-red product was precipitated out of this oxidized compound when 150 ml of distilled water was added. The product was filtered, dried, and fully oxidized by dispersing it in a 5% hydrogen peroxide solution. Centrifugation was used to separate the bright red product, which was then vacuum-dried for 12 hours. The synthesis reaction resulted in the formation of 1.5 grams of a bright red product, with a yield of 37.5 percent. The product was washed with acetone and characterised by IR (Figure S4) and ^{1}H (Figure S5) and ^{13}C NMR (Figure S6) studies.^{1}H-NMR (DMSO-d_6, 400 MHz): δ= 8.08 (d, 4H), 6.68 (d, 4H), 5.91 (s, 4H), ^{13}C-NMR (DMSO-d_6, 125 MHz):162.83, 152.61, 129.09, 119.36, 114.77.

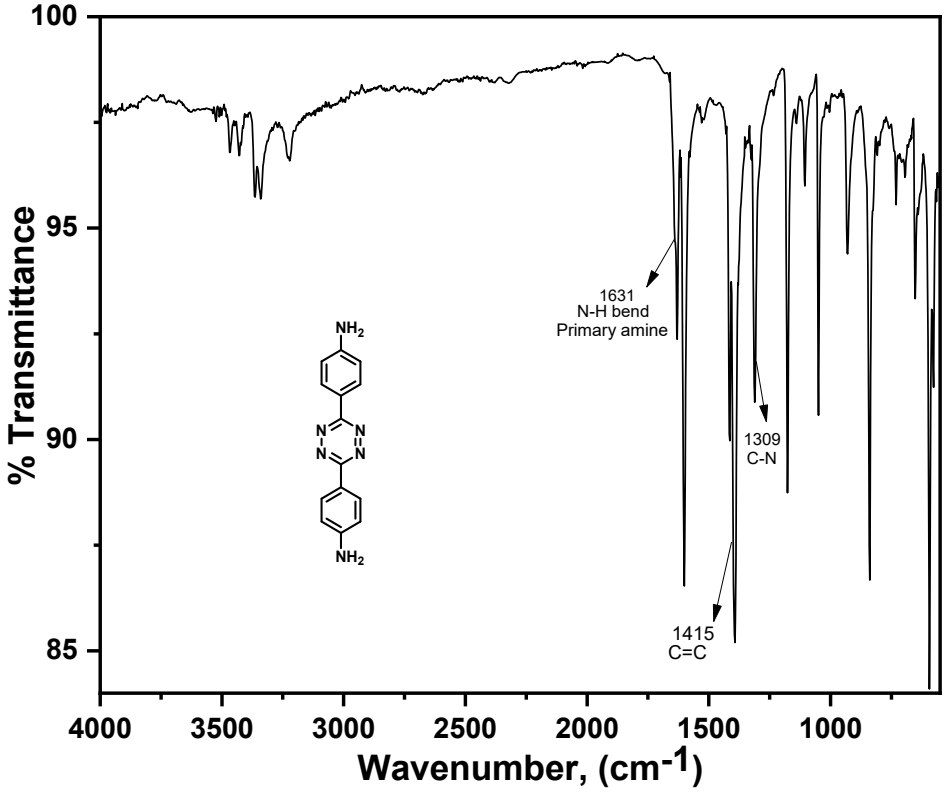

Figure S4. Fourier transform infrared spectrum of s-tetrazine diamine (Tz).

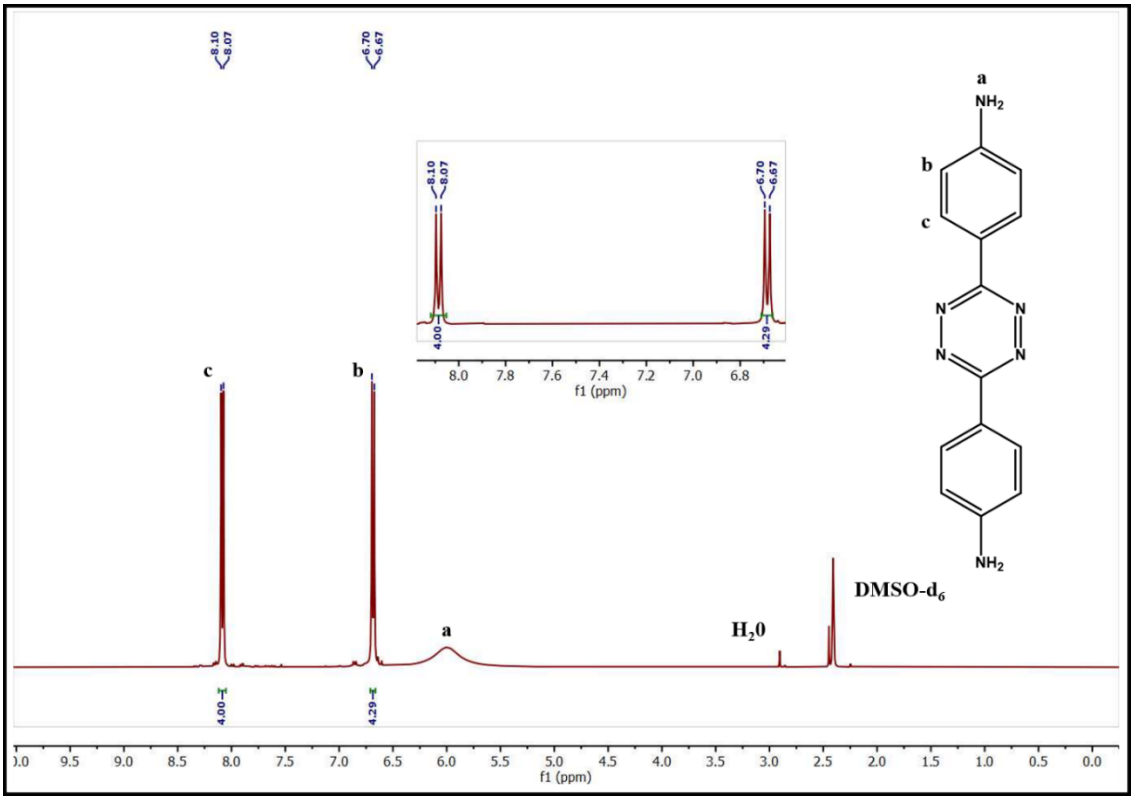

Figure S5. ^{1}H NMR spectrum of s-tetrazine diamine (Tz) in DMSO-d_6 (400 MHz).

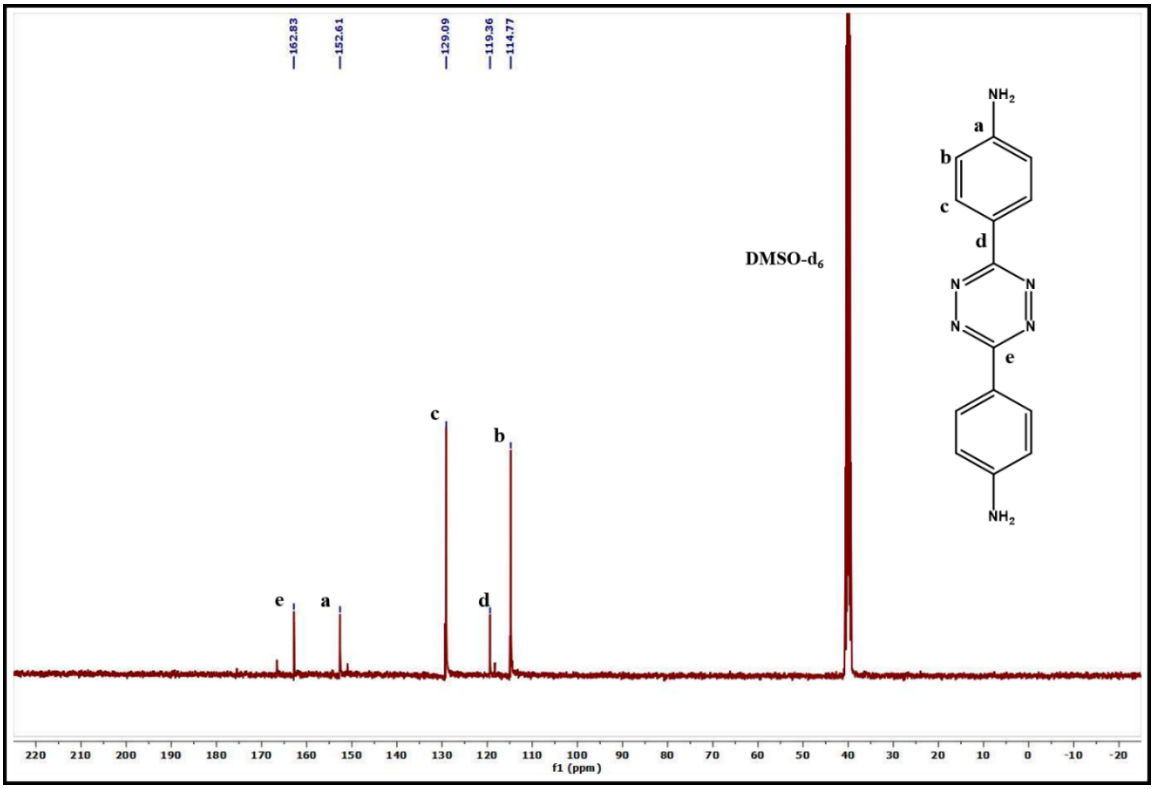

Figure S6. ^{13}C NMR spectrum of s-tetrazine diamine (Tz) in DMSO-d_6 (400 MHz).

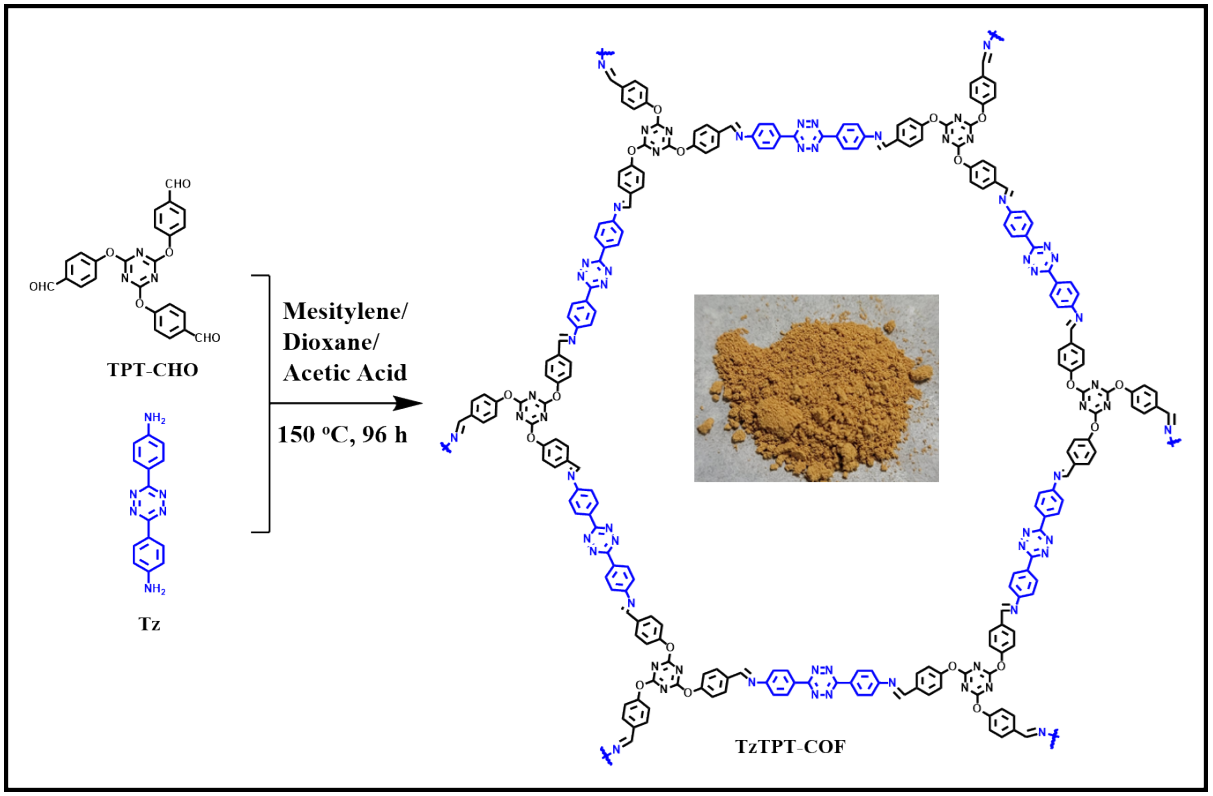

Scheme S3. Synthesis of TzTPT-COF from corresponding monomer Tz and TPT-CHO.

Synthesis of TzTPT-COF: TPT-CHO (132 mg, 0.3 mmol) and s-tetrazine-diamine (118 mg, 0.45 mmol) were dissolved in a mixture of 6.0 mL of dioxane and 6.0 mL of mesitylene and stirred until homogenization was achieved, resulting in a red solution. Subsequently, 1.0 mL of a 0.6 M acetic acid was added to the mixture. The Pyrex tube containing the reaction mixture was flash-frozen in liquid nitrogen and sealed before being subjected to thermal treatment at 150 °C for 4 days, followed by a slow cooling to room temperature over a period of 12 hours. This process yielded approximately 170 mg of a bright yellow coloured solid, which was subsequently washed with hot DMF, dioxane, MeOH, acetone, and THF (68%, isolated yield).

S4. CHN analysis of TzTPT-COF

Table S1. CHN analysis of TzTPT-COF:

Mol. Weight (g/mol)	**Formula**		**C**	**H**	**N**
4096.13	$C_{234}H_{156}N_{60}O_{18}$	**Calculated**	68.61%	3.84%	20.52%
		Obtained	66.171%	3.455%	18.815%

S5. FTIR spectrum of TzTPT-COF

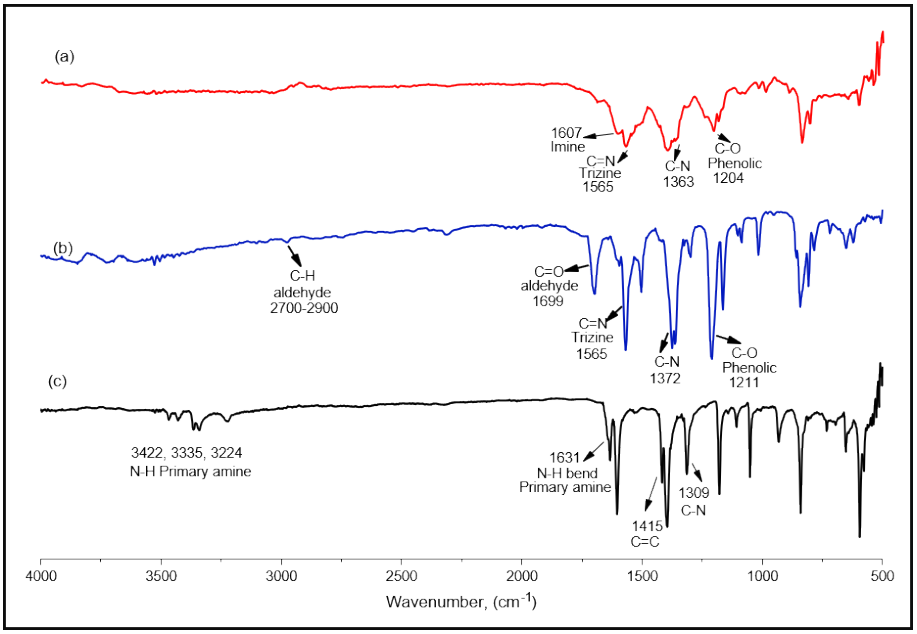

Figure S7. FTIR spectra of (a) TzTPT-COF, (b) TPT-CHO and (c) s-tetrazine-diamine (Tz).

S6. TGA of TzTPT-COF

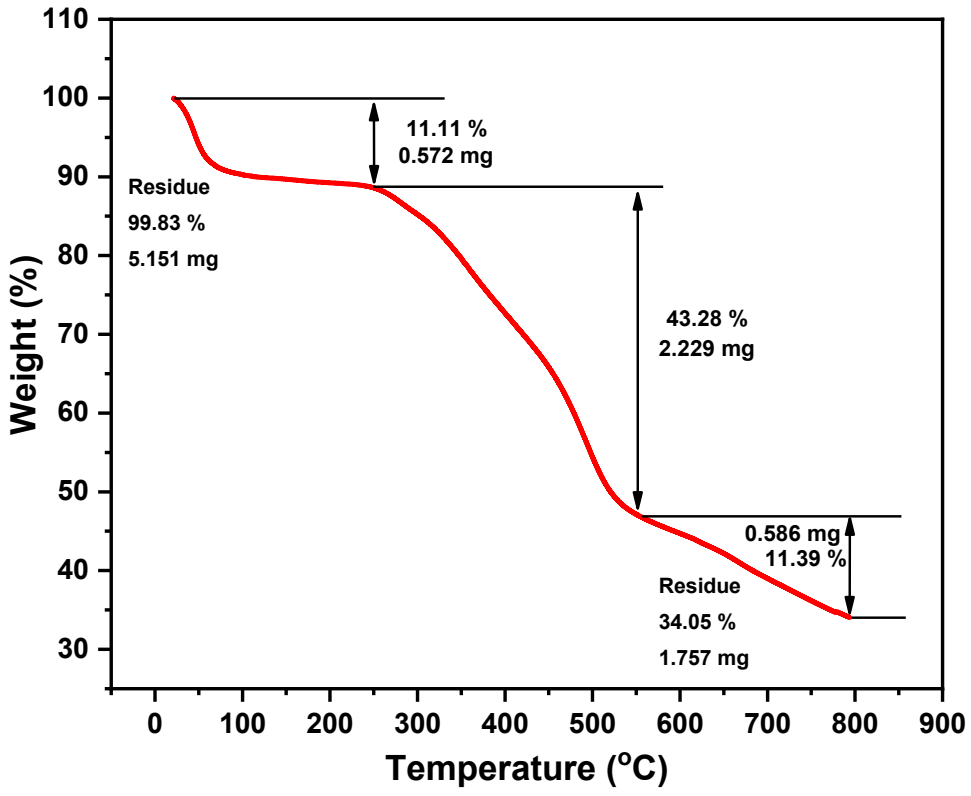

Figure S8. TGA of TzTPT-COF under N_2 flow with a heating rate of 10 °C/min.

S7. PXRD of the COF

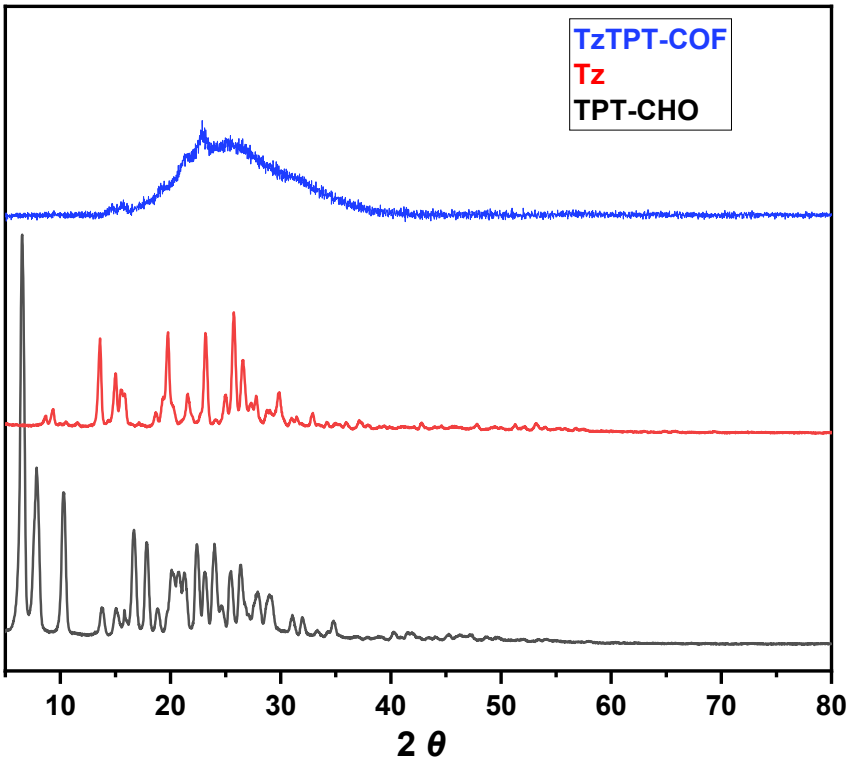

Figure S9. Comparative PXRD patterns of the TPT-CHO, Tz Precursors and TzTPT-COF.

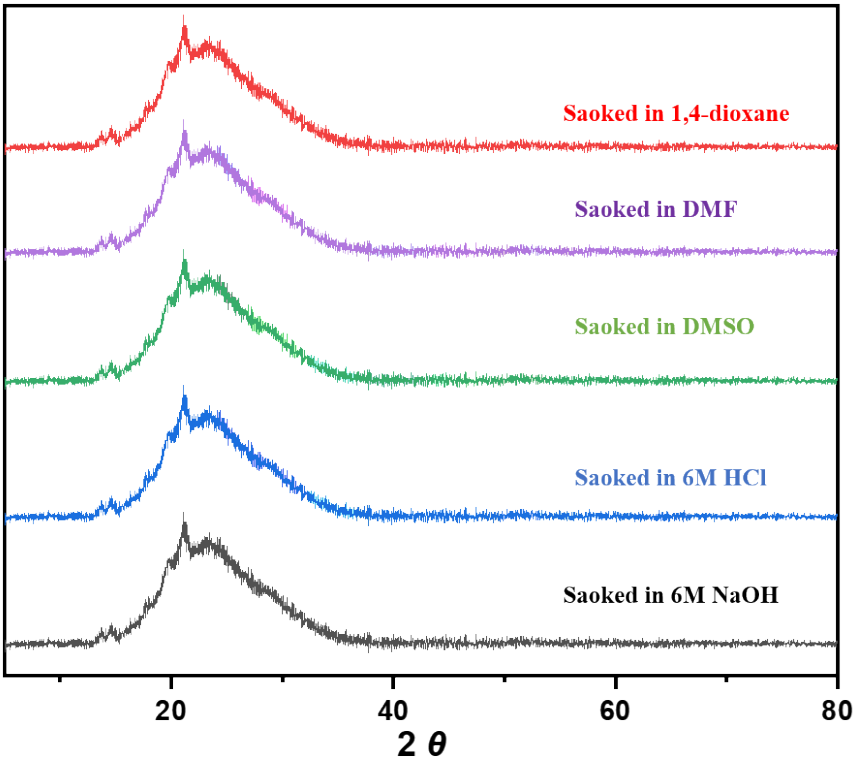

Figure S10. PXRD patterns of TzTPT-COF after soaking in different solvents.

S8. Field Emission Scanning Electron Microscopy (FE-SEM)

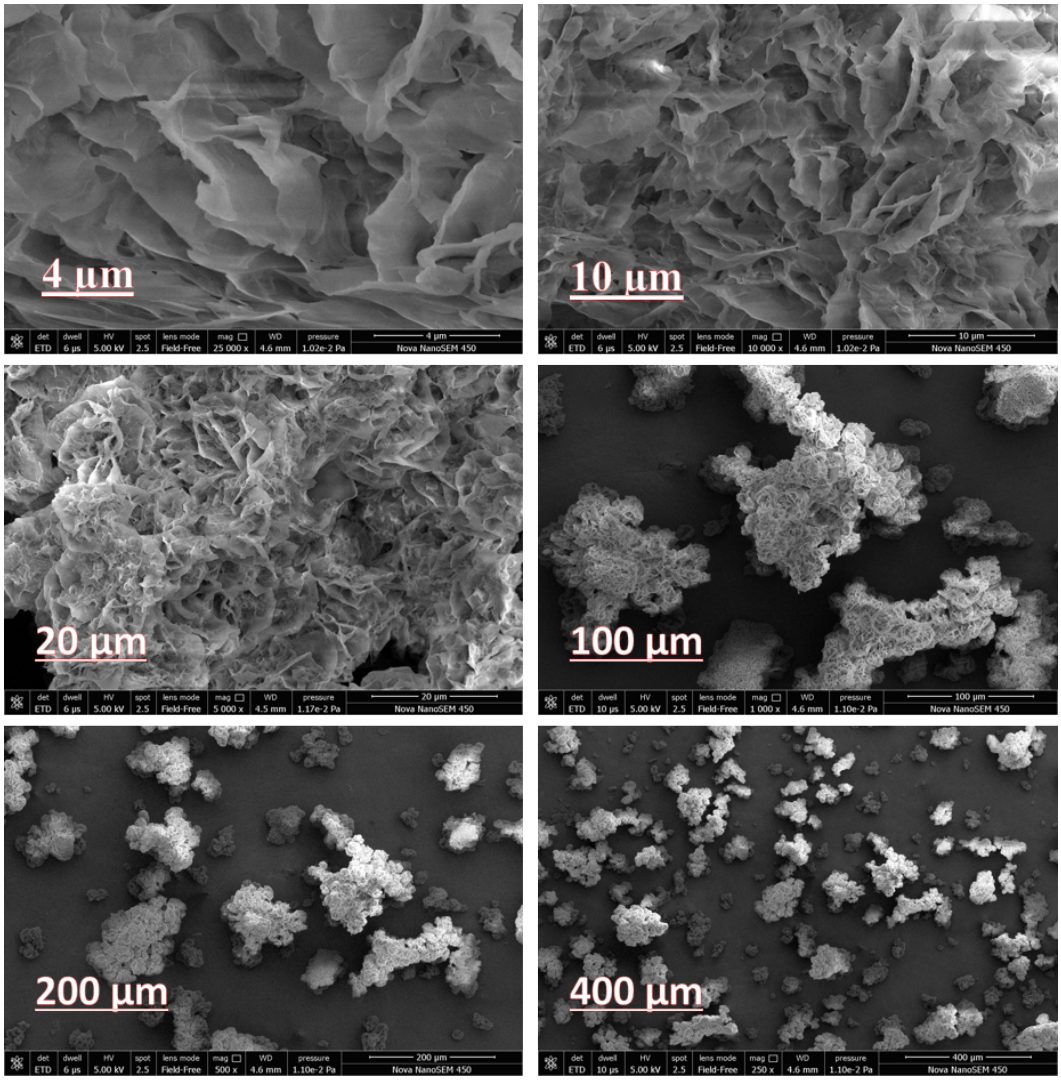

Figure S11. FE-SEM images of TzTPT-COF at different resolutions. Shows flaky morphology. At lower resolution, a fluffy cotton-like morphology can be seen. Whereas at higher resolution, the presence of aggregated-flakes can be seen.

S9. High Resolution Transmission Electron Microscopy (HR-TEM)

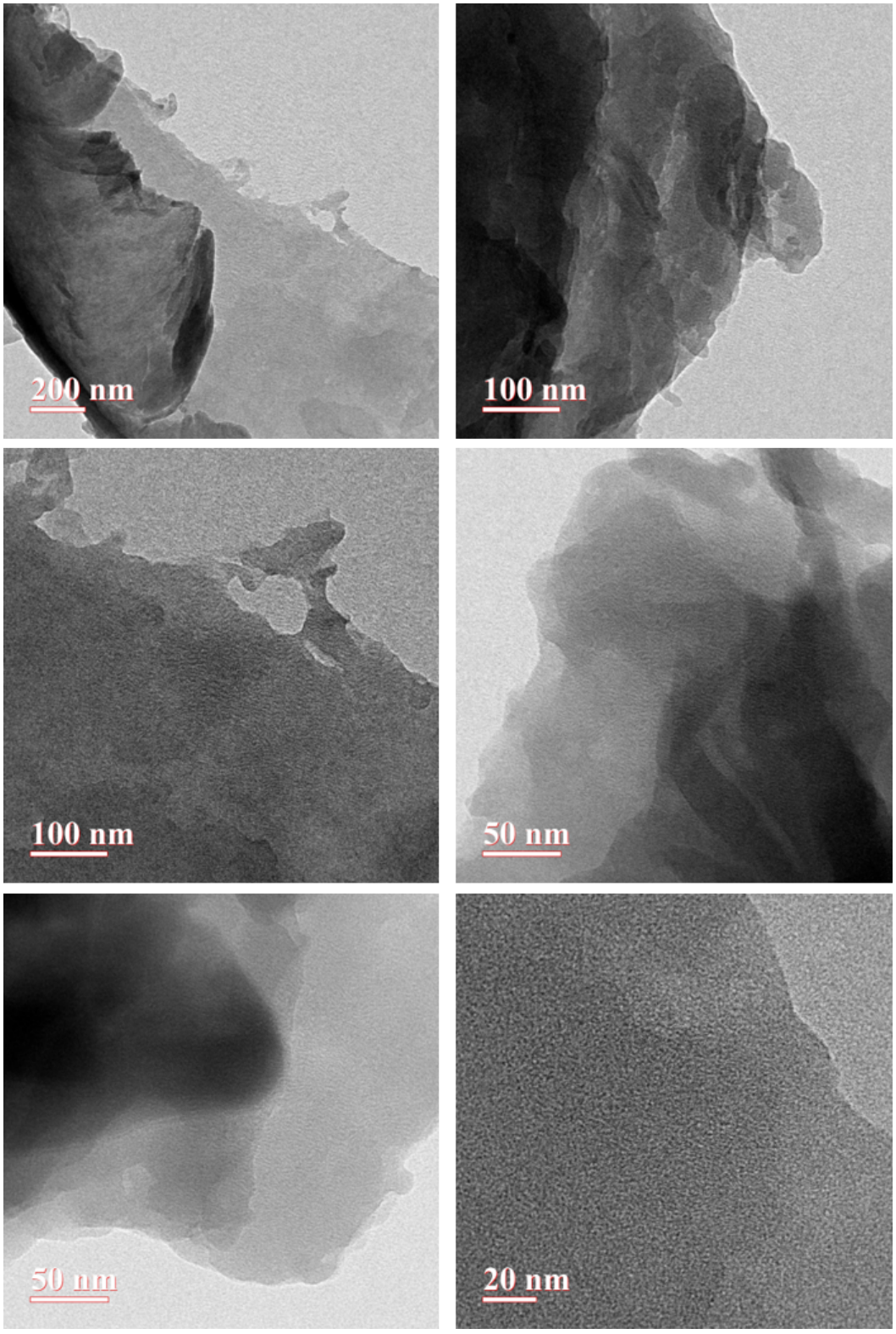

Figure S12. HR-TEM images of the TzTPT-COF under different magnifications showing the aggregates formed by stacking of many sheets. Darker regions are from such multi-flake

stacking. While at 20 nm resolution the uniform micropores all along the surface of the COF can be seen.

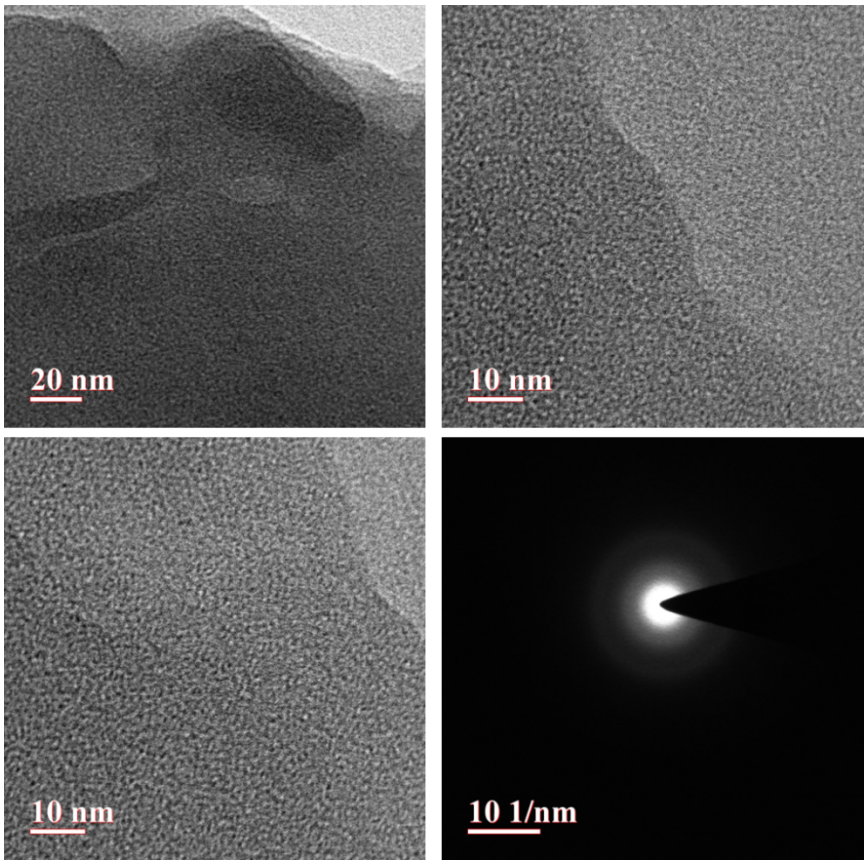

Figure S13. HR-TEM images of the TzTPT-COF under higher magnifications and SAED pattern of TzTPT-COF.

S10. Dye Adsorption Study with TzTPT-COF

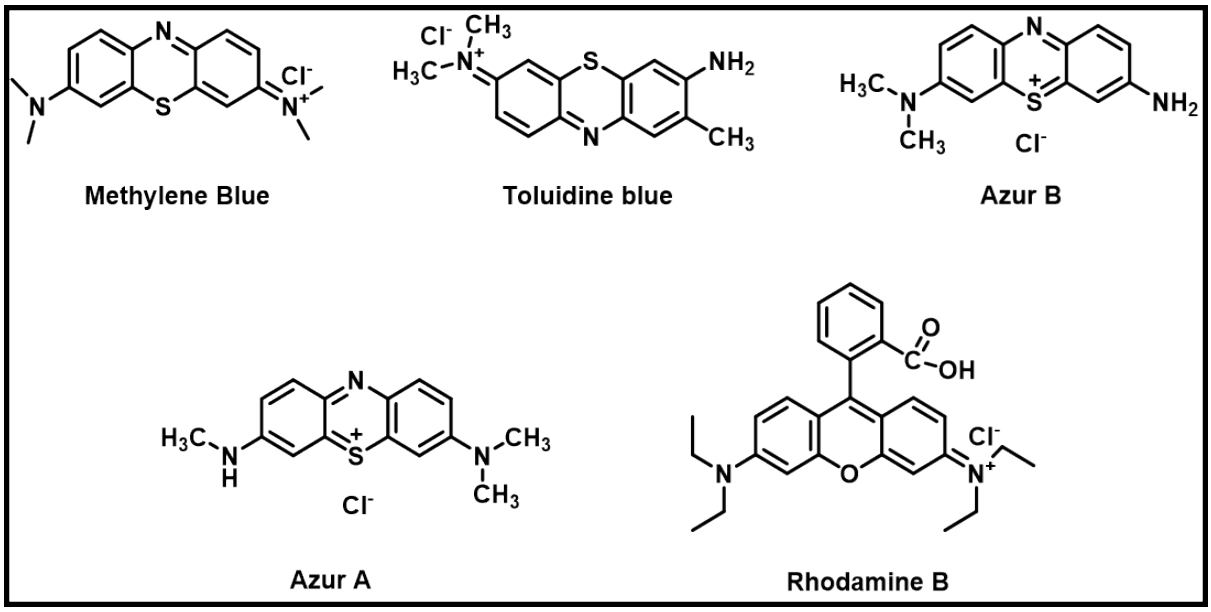

Figure S14. Chemical structures of the different dyes tested for adsorption with the TzTPT-COF.

Various organic dyes including Methylene Blue (MB), Azure A (AZA), Azure B (AZB), Toluidine blue O (TOLO), and Rhodamine B (RHB) were selected to study the adsorption ability of TzTPT-COF. In a typical experiment, an aqueous solution of MB, TOLO, RhB, AZA, and AZB (10 mL) was mixed with 5 mg of TzTPT-COF, and the mixture was then agitated at 500 rpm for 0-60 minutes. The UV-visible spectroscopy was used to measure the absorbance of dyes at the maximum absorbance wavelength for both before and after adsorption processes. Methylene blue (MB) aqueous dye concentrations (ranging from 10 to 600 mg L^{-1}) were employed to create adsorption isothermal curves. In each experiment, (5 mg) of TzTPT-COF was added to a (10 ml) aqueous solution of MB in a glass vial. The mixture was then subjected to stirring at a rotational speed of (500 rpm) for a duration of 120 minutes. The isothermal curve was created by centrifuging the supernatant and recording its UV-Vis spectrum. The kinetic experiments of TzTPT-COF with MB were conducted to learn more about the adsorption characteristics of the substance. In this study, MB (300 mg L^{-1}) at various time intervals from 5 to 150 minutes has been used. The reusability of TzTPT-COF for adsorption was evaluated by adding 5 mg of the material to a 10 mL aqueous solution containing 300 mg L^{-1} of dye. The mixture was stirred for 1 hour and the supernatant was collected and analyzed using UV-Vis spectroscopy to determine the efficiency of adsorption. To remove the adsorbed dye, the exhausted TzTPT-COF was washed repeatedly with water, methanol, and acetone. The regenerated TzTPT-COF was utilised in the subsequent dye removal test after being dried overnight at 100 °C. For calculating the removal efficiency (%RE), adsorption amount Q_t (mg g^{-1}), and equilibrium adsorption capacity Q_{eq} (mg g^{-1}) of dyes, below given equations were used:[3]

$$Removal\ (\%) = \frac{C_0 - C_t}{C_0} \times V$$

$$Q_t = \frac{C_0 - C_t}{m} \times V$$

$$Q_{eq} = \frac{C_0 - C_{eq}}{m} \times V$$

Where C_0, C_t, and Ce (mg L^{-1}) are dye concentrations at the initial time, a given time t, and equilibrium in the solution, respectively. V (L) represents the volume of the solution, and m (g) is the mass of the adsorbent (g).

The empirical Freundlich model, which is recognised as being suitable for low concentrations, is stated by following equation:[4]

$$Q_{eq} = K_F C_e^{1/n}$$

where K_F ((mg g^{-1})/(mg L^{-1})1/*n*) is the Freundlich constant relating to adsorption capacity and *n* is the intensity. In order to determine the Freundlich constant, above Equation can be linearized to its logarithmic version as shown below.

$$\ln Q_{eq} = \ln K_F + \frac{1}{n} \ln C_{eq}$$

The following equation describes the Langmuir isotherms model:[5]

$$Q_{eq} = \frac{Q_m K_L C_{eq}}{1 + b C_{eq}}$$

where Q_m (mg g^{-1}) is the maximum adsorption capacity, and K_L (L mg^{-1}) is the Langmuir constant.

The following is an expression for the Langmuir equation's linear form:

$$\frac{C_{eq}}{Q_{eq}} = \frac{1}{K_L Q_m} + \frac{C_{eq}}{Q_m}$$

Regression coefficients (R^2) and constants for the Langmuir and Freundlich isotherm models are compiled in Table S2.

The adsorption kinetic behaviour of TzTPT-COF over MB was estimated using two well-known adsorption models, the pseudo-first-order and pseudo-second-order kinetic models.[6]

The pseudo-first-order kinetics equation is given below:

$$\ln (Q_{eq} - Q_t) = \ln Q_{eq} - k_1 t$$

where Q_{eq} and Q_t are the adsorption capacity (mg g^{-1}) at equilibrium and at a given time t (min), respectively, and k_1 is the rate constant for the pseudo-first-order adsorption (min^{-1}). The pseudo-second-order kinetics equation is given below:

$$\frac{dQ_t}{dt} = k_2(Q_{eq} - Q_t)^2$$

$$\frac{t}{Q_t} = \frac{1}{k_2 Q_{eq}^2} + \frac{t}{Q_{eq}}$$

where k_2 is the rate constant of pseudo-second-order adsorption (g mg^{-1} min^{-1}).

The adsorption isotherm were studied for MB on TzTPT-COF at room temperature (RT), 40 °C, and 50 °C in the initial concentration range 10 to 600 mg L^{-1} (Fig. S15). The adsorption capacity of methylene blue (MB) exhibited an upward trend as the initial concentration of MB increased, suggesting a favorable adsorption behavior of MB on the TzTPT-COF material, particularly at higher concentrations. In order to determine the maximum adsorption capacity of MB, the adsorption isotherms were analyzed and fitted using the Langmuir model. The plots of C_{eq}/Q_{eq} against C_{eq} gave good linear plots at all of the test initial concentrations, indicating the adsorption of MB follows the Langmuir model. With increasing temperature, the maximum adsorption capacity of MB on TzTPT-COF exhibited a notable enhancement from 398.434 mg g^{-1} to 572.478 mg g^{-1} (Table S4). This observation indicates the favorable nature of MB adsorption on TzTPT-COF, particularly at higher temperatures. Hence, this novel amorphous TzTPT-COF adsorbent can be strongly recommended as an efficient alternative for the removal of dyes. The adsorbed amount Q_t on TzTPT-COF vs. time for various initial dye concentrations (50, 100, and 300 mg L^{-1}) are shown in Fig. S16. The adsorption kinetics of the dye demonstrate a rapid initial uptake at varying concentrations, which progressively diminishes over time until reaching a state of equilibrium. The initial stage of adsorption exhibited a higher rate attributed to the greater abundance of active sites on the TzTPT-CHO surface. Nevertheless, as the process advanced, these active sites became progressively occupied by the dye molecules, leading to a reduction in available adsorptive sites for the remaining dye molecules in the solution. The findings further demonstrated a direct correlation between the initial dye concentration and the amount of dye adsorbed onto TzTPT-COF. Specifically, the equilibrium adsorbed quantity of dye onto TzTPT-COF increased from 106.0796 mg g^{-1} to 385.9453 mg g^{-1} as the initial concentrations of MB increased from 50 mg L^{-1} to 300 mg L^{-1}. The plots of t/Q_t versus time for various initial dye concentrations exhibit a remarkable linear relationship, as depicted in Fig. S16. The outcomes reveal that the pseudo second-order kinetic model provides a superior fit to the experimental data, as evidenced by the linear regression coefficients of 0.999 ($R^2 > 0.999$) observed across all initial dye concentrations (Table S5). UV-Vis spectra of an aqueous MB solution (initial concentration: 10 mg L^{-1}) after 30 minutes after the addition of the (a) Tz, (b) TPT-CHO and (c) Mixture of Tz and TPT-CHO as illustrated in Fig. S17. MB adsorption capability of TZ, TPT-CHO and their physical mixture is very less or almost negligible. In case of TPT-CHO the adsorption capability is 7.24%, in case of Tz the adsorption capability is 13.58% and in case of mixture the adsorption capability is 10.78 %. In comparison to other reported adsorbent polymers such as OMC, MOFs, CMPs, as well as various natural adsorbents listed in Table S9, the adsorption capacity of amorphous

TzTPT-COF for MB demonstrates its remarkable potential as one of the most promising adsorbent. Several comparision plots between adsorption capacity of TzTPT-COF with other reported adsorbents polymers such as OMC, MOFs, CMPs as well as various natural adsorbent exhibited in Fig. S26, S27, S28 and S29. These plots serve as a scientific basis for assessing the effectiveness of TzTPT-COF in comparison to other materials for adsorption purposes. As shown in Fig.3, both MB and RhB are of cations dyes, while MB has been removed very quickly and RhB was there almost with no variation after 1 hour. To understand the reason kinetic study of RhB was conducted at different initial concentration mentioned in Fig. S18 and Table S6 and computational simulations were employed to complement the experimental findings. To get a better insight of the adsorption behaviour of the two cationic dyes MB and RhB, the Energy decomposition Analysis has been done which gives the total interaction between the fragments (Dye and COF) in terms of interaction energy.

The interaction energy is further decomposed into various contributions,

$$\Delta E_{int} = \Delta E_{elst} + \Delta E_{Pauli} + \Delta E_{orb} + \Delta E_{disp}$$

where, the term ΔE_{elst} corresponds to the electrostatic interaction (attractive in nature), ΔE_{Pauli} refers to the Pauli repulsion energy, $\Delta E_{orbital}$ accounts for orbital interactions resulting from electron pair bonding, charge transfer and polarization terms, and ΔE_{disp} represents the dispersion interaction terms.

From the EDA analysis values mentioned in Table S7, it can be concluded that between the two dyes MB and RhB, the ΔE_{int} value is higher (~2.27 times) for MB@ TzTPT-COF as compared to the RhB@ TzTPT-COF. The $\Delta Eorb_{(1)}$ value for MB@ TzTPT-COF is also comparatively larger than RhB@ TzTPT-COF which can be clearly seen in Fig. S19. Moreover, the two bulky ethyl ($-CH_2CH_3$) groups on N and extra benzene ring with –COOH group of RhB might cause some steric hindrance for the RhB dye to come in direct contact with the TzTPT-COF, whereas MB has comparatively smaller methyl groups on N as evidenced via the NOCV difference density plots shown in Fig. S19.

Table S2. Isotherm parameters for the adsorption of MB on TzTPT-COF.

Adsorbent	**Langmuir (linear)**			**Freundlich (linear)**		
	Q_{max}	K_L	R_L^2	K_F	n	R_F^2
TzTPT-COF	398.434 mg g^{-1}	0.15829	0.9986	90.85753	3.5504556	0.7206

Table S3. Kinetic parameters for the adsorption of MB on TzTPT-COF.

Initial concentration	**Pseudo-first-order kinetic model**			**Pseudo-second-order kinetic model**		
	k_1 **(1/h)**	Q_e, **(mg** g^{-1}**)**	R^2	k_2 **(g** mg^{-1} min^{-1}**)**	Q_e, **(mg** g^{-1}**)**	R^2
300 mg L^{-1}	0.001008667	3.7831E-158	0.8846	0.000599	385.9453	0.9997

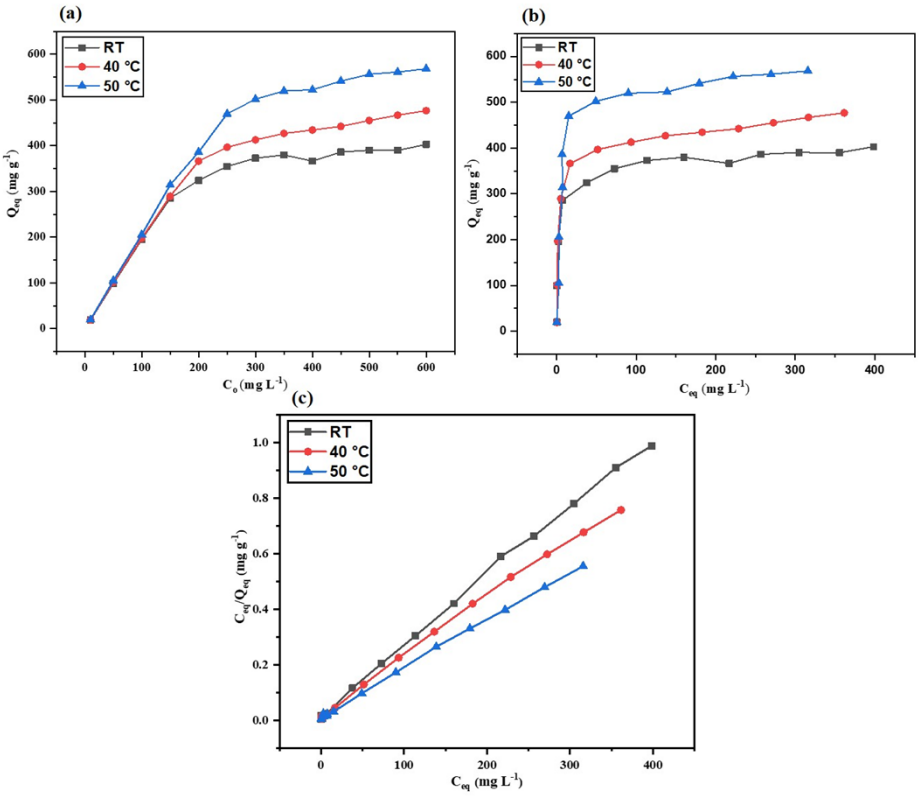

Figure S15. The adsorption isotherm for MB on TzTPT-COF (a) Q_{eq} vs C_o, (b) Q_{eq} vs C_{eq} at room temperature (RT), 40 °C, and 50 °C, and the corresponding Langmuir plot for MB (c).

Table S4. Isotherm parameters for the adsorption of MB on TzTPT-COF at different temperatures.

Adsorbent	**Temperature**	**Langmuir (linear)**		
TzTPT-COF		**Q_{max}**	**K_L**	**R_L^2**
	RT	398.434 mg g^{-1}	0.15829	0.9986
	40 °C	471.634 mg g^{-1}	0.13542	0.9978
	50 °C	572.478 mg g^{-1}	0.15121	0.999

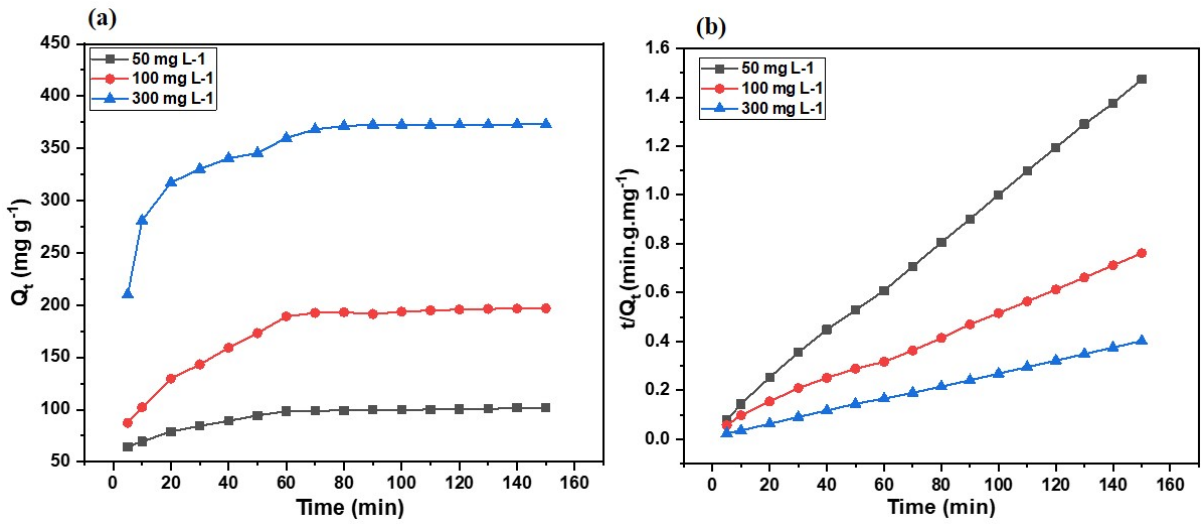

Figure S16. (a) Pseudo-second-order kinetic model plots for the adsorption of MB on TzTPT-COF at different initial concentrations, (b) Fitting curve of adsorption on MB through Pseudo-second-order kinetic model.

Table S5. Kinetic parameters for the adsorption of MB on TzTPT-COF at different initial concentrations.

Initial concentration	**Pseudo-second-order kinetic model**		
	k_2 (g mg^{-1} min^{-1})	Q_e, (mg g^{-1})	R^2
50 mg L^{-1}	0.001524	106.0796	0.9996
100 mg L^{-1}	0.000402	214.8177	0.9979
300 mg L^{-1}	0.000599	385.9453	0.9997

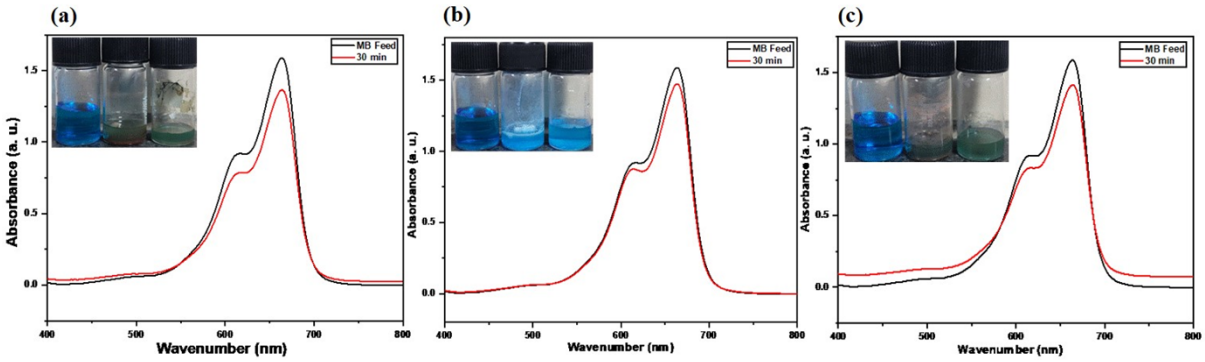

Figure S17. UV-Vis spectra of an aqueous MB solution (initial concentration: 10 mg L^{-1}) after 30 minutes after the addition of the (a) Tz, (b) TPT-CHO and (c) Mixture of Tz and TPT-CHO.

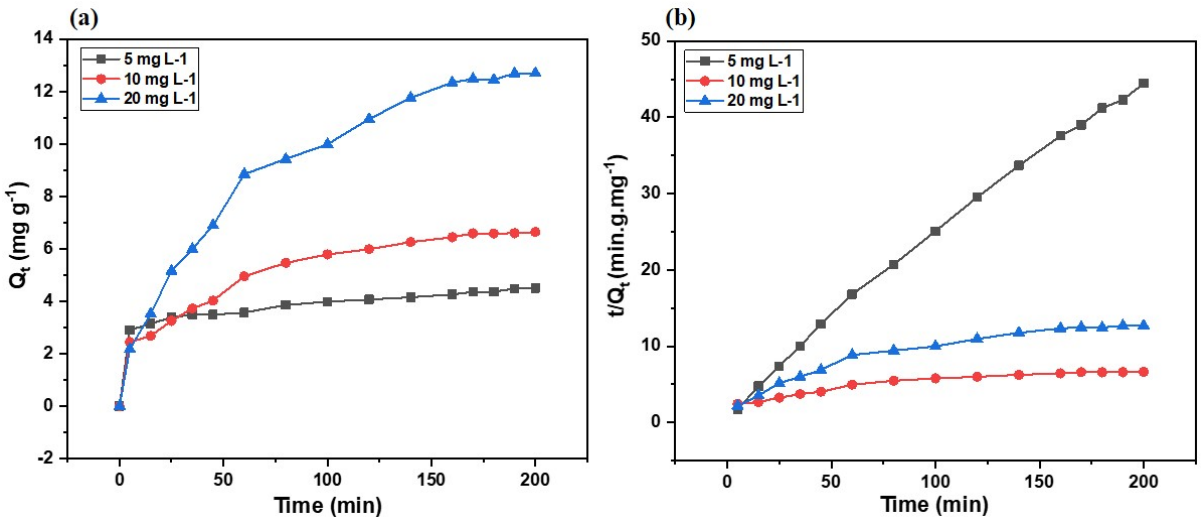

Figure S18. (a) Pseudo-second-order kinetic model plots for the adsorption of RhB on TzTPT-COF at different initial concentrations, (b) Fitting curve of adsorption on RhB through Pseudo-second-order kinetic model.

Table S6. Kinetic parameters for the adsorption of RhB on TzTPT-COF at different initial concentrations.

Initial concentration	**Pseudo-second-order kinetic model**		
	k_2 (g mg^{-1} min^{-1})	**Q_e, (mg g^{-1})**	**R^2**
5 mg L^{-1}	0.018767	4.62361	0.9954
10 mg L^{-1}	0.00448	7.59681	0.9914
20 mg L^{-1}	0.001227	15.9487	0.9902

Table S7. EDA-NOCV energies computed at PBE-D3BJ/TZP level of the theory for MB and RhB dyes adsorbed on TzTPT-COF. All the values are in kcal/mol.

Energy	**MB**	**RhB**
ΔE_{int}	-19.72	-8.68
ΔE_{Pauli}	12.93	5.11
ΔE_{disp}	-12.55	-7.18
ΔE_{elstat}	-11.37	-3.63
ΔE_{orb}	-8.73	-2.98

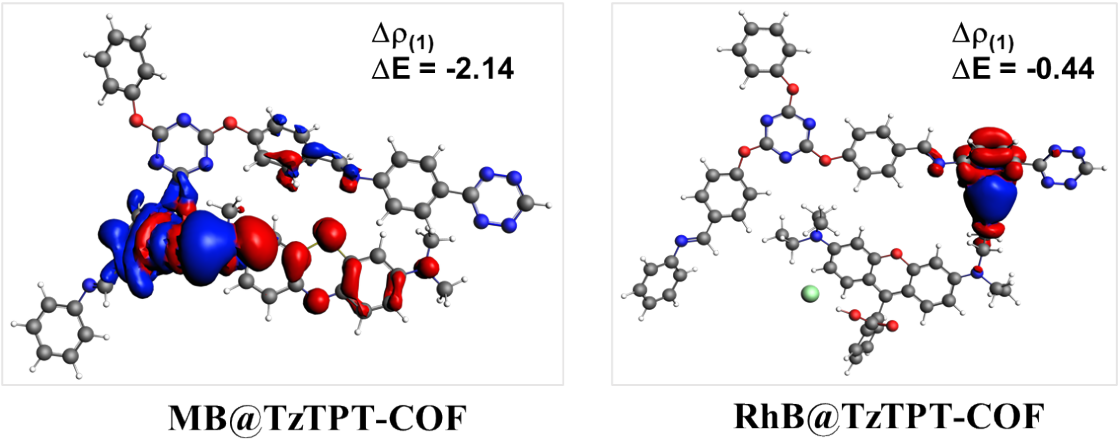

Figure S19. Plot of electron deformation densities (EDD) corresponding to the highest interaction $\Delta Eorb_{(1)}$ for MB@ TzTPT-COF and RhB@TzTPT-COF.

S11. Reusability test

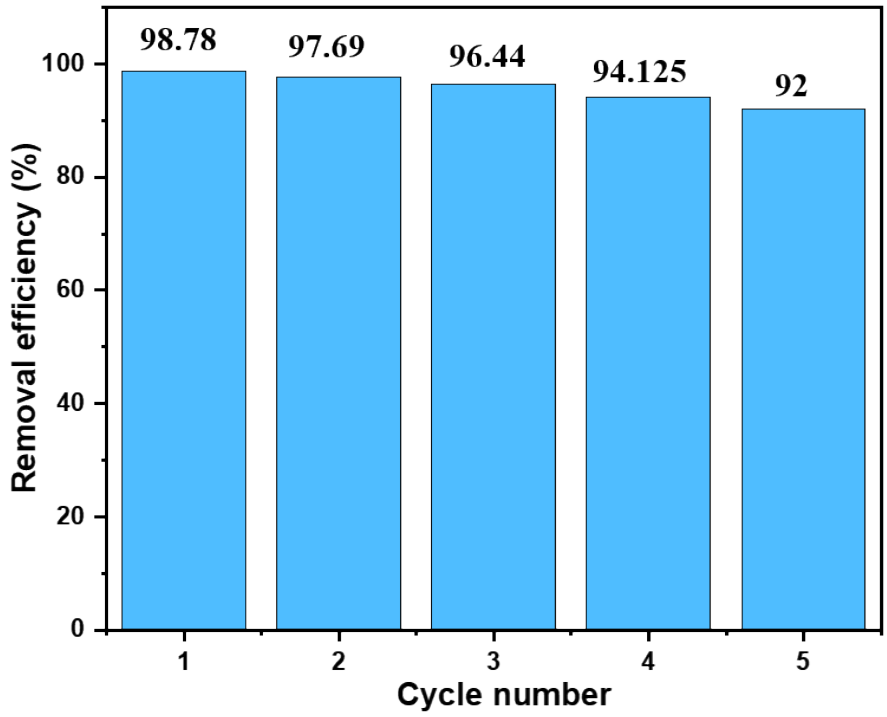

Figure S20. Reusability of the TzTPT-COF for the removal of MB within 20 min.

S12. Chemical stability of TzTPT-COF

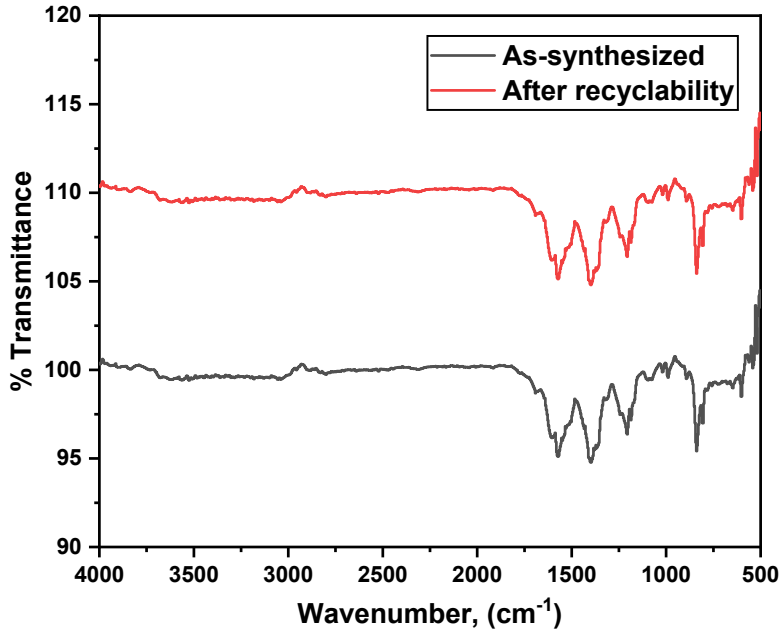

Figure S21. FT-IR spectra of TzTPT-COF as-synthesized, after recyclability from dye experiments.

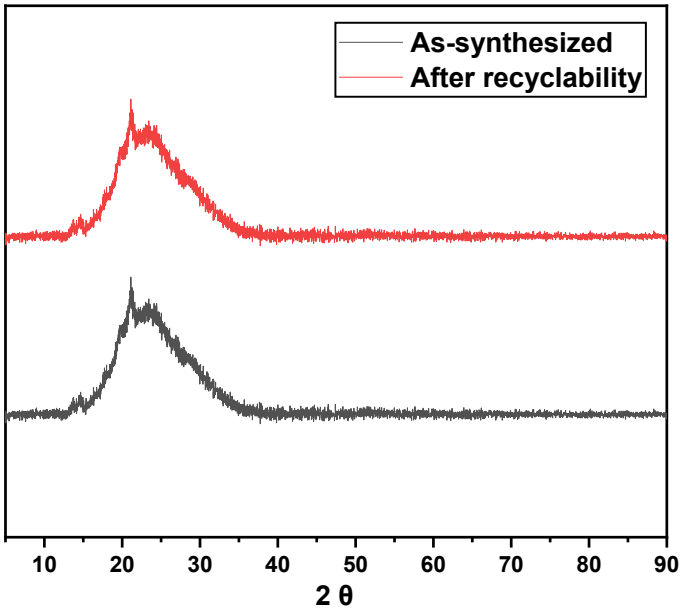

Figure S22. PXRD spectra of TzTPT-COF as-synthesized, after recyclability from dye experiments.

S13. Modeling and Theoretical Simulations

All calculations have been performed using the density functional theory (DFT) in a periodic framework, as implemented in VASP 5.4.4. The projector augmented wave (PAW) method was used to describe the frozen core electrons and their interaction with the valence electrons.

The electronic wave function was expanded in plane waves up to a cutoff energy of 520 eV. Gamma-centred 2×2×1 k-points were used in the Brillouin zone corresponding to the primitive cell. The Perdew–Burke–Ernzerhof functional (PBE) has been used along with the dispersion interactions (DFT-D3) proposed by Grimme et al.[7]

Presence of a lot of aromatic rings and typically cationic nature of dyes with planar structure, they bound together π-π stacking interactions. COF acts as electron-donating Lewis base,whereas the cationic dye is viewed as a Lewis acid due to the fact that COF contains a significant quantity of electron-rich atoms like N and O (carrying a lone pair of electrons). Hence, these N and O atoms can draw cationic dye molecules during the adsorption process, in accordance with the Lewis acid-base reaction theory which is evident from the charge difference density plot. The adsorption process also results in changes in the structure of MB molecule from a curved geometry to a somewhat linear form, showing a stronger electrostatic interaction (Fig. 7).

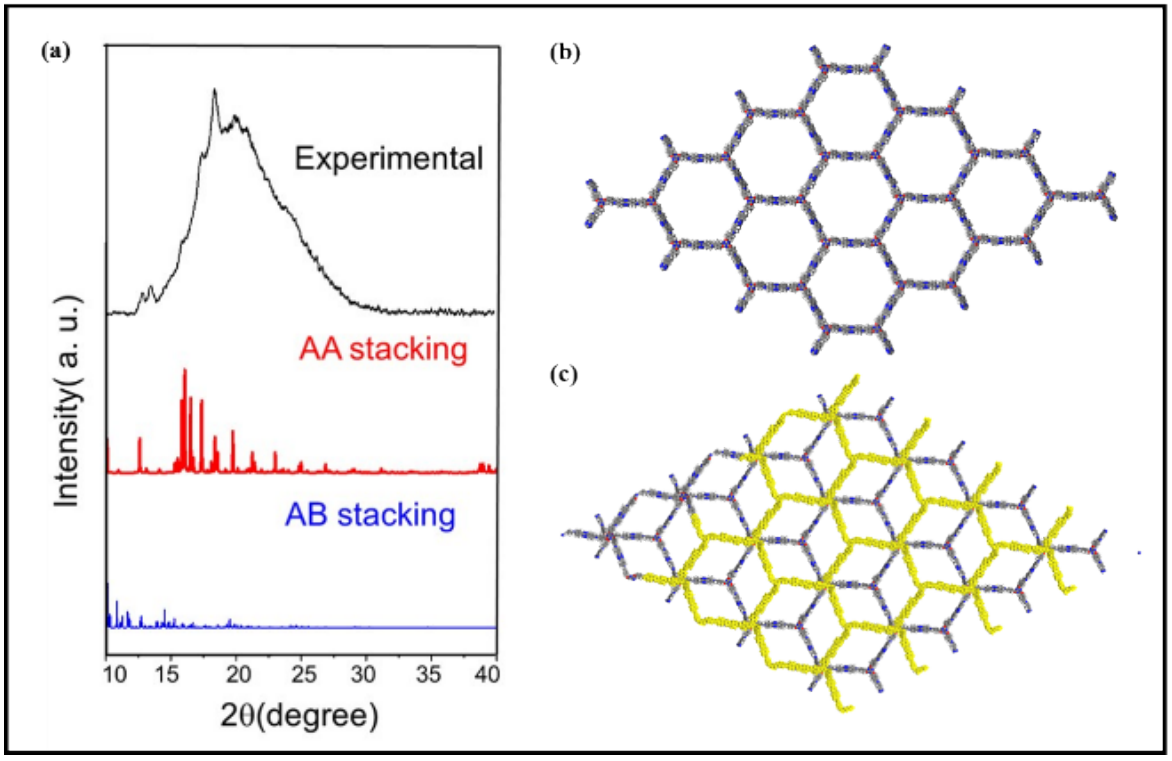

Figure S23. (a) Powder X-ray diffraction study of TzTPT-COF. Experimental (black line), simulated AA-stacking model (red line) and AB-stacking model (blue line). (b) eclipsed AA-stacking model. (c) Staggered AB-stacking model.

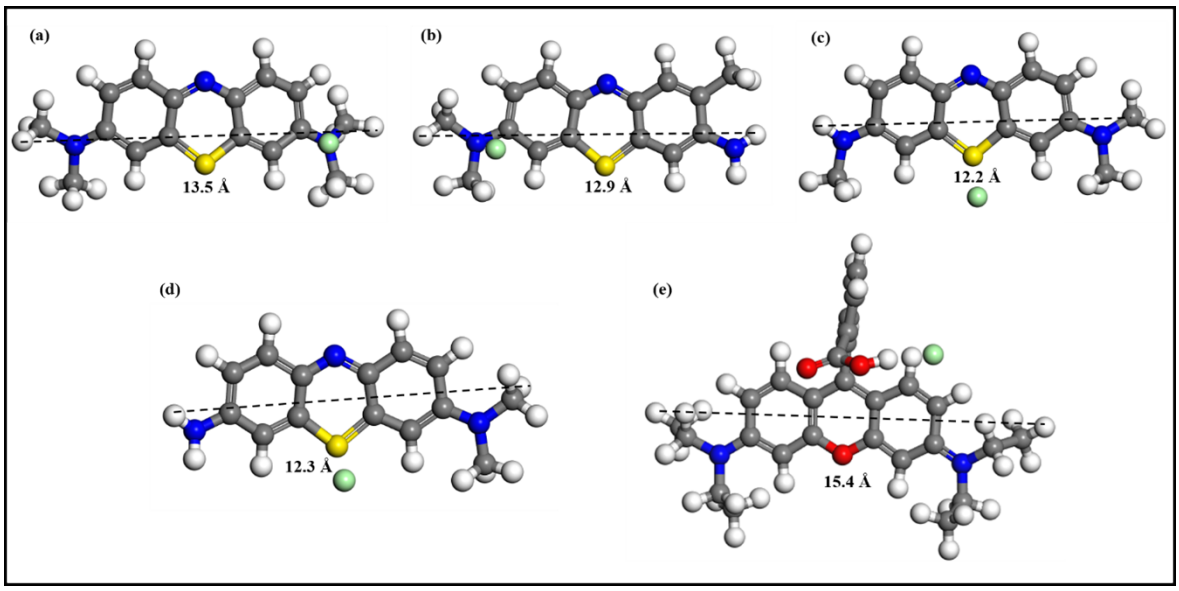

Figure S24. DFT-optimized structures of dyes (a) MB, (b) TOLO, (c) AZA, (d) AZB, (e) RhB. Color codes: C (grey); H (white); N (blue); O (red); Cl (green); S (yellow).

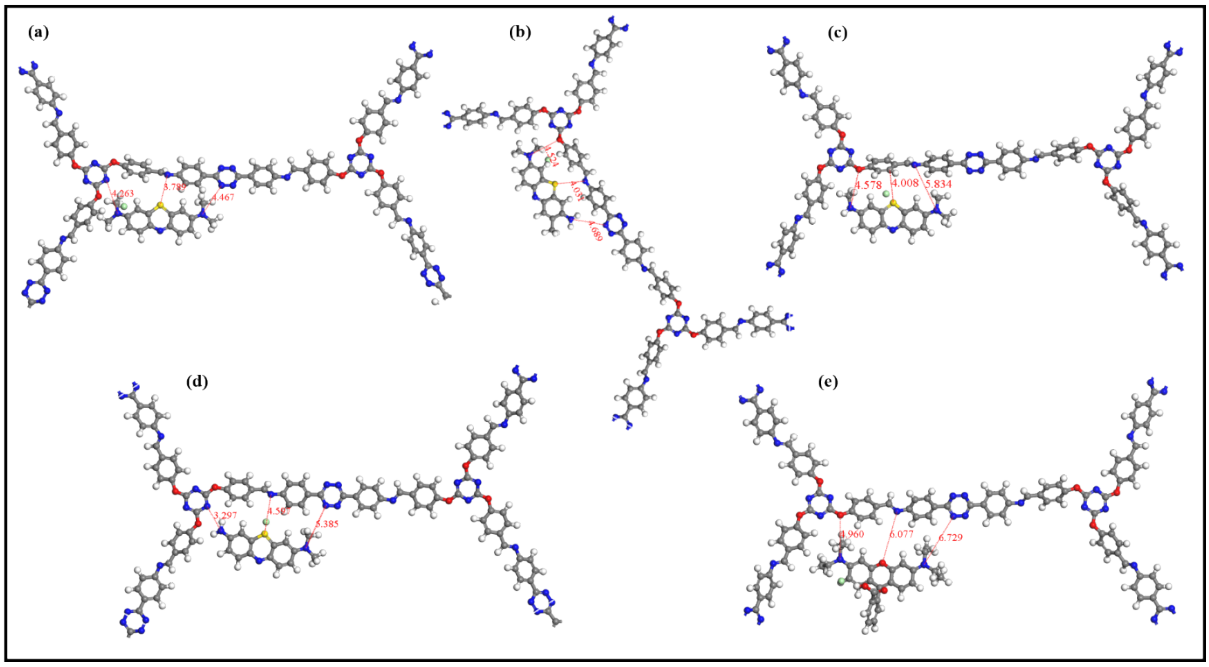

Figure S25. DFT-optimized structures of respective dyes absorbed on TzTPT-COF (a) MB (b) TOLO (c) AZA (d) AZB (e) RhB. Color codes: C (grey); H (white); N (blue); O (red); Cl (green); S (yellow).

Table S8: Cartesian atomic coordinates for the smallest unit cell of TzTPT-COF.

Space group: P6(C6-1)			
a = 53.575702 Å b = 53.575702 Å c = 6.9372 Å			
α = 90°, β = 90°, γ = 120°			
N	27.472011689000	15.849528524242	3.327081120000
N	25.360593352000	14.740618302552	3.100442796000
N	25.442028416000	17.113407789466	3.251951244000
N	13.566974511000	23.997930747391	2.738598444000
N	12.346520065000	21.985189098147	3.159062136000
N	12.438670269000	24.679980130606	2.743315740000
N	11.226520056500	22.665846543846	3.178902528000
N	6.378990720500	26.854650510967	3.400962300000
N	18.152250795500	19.418920296403	3.033776304000
N	39.462789106000	22.465871520604	4.850420868000
N	38.192509259000	24.417367919109	4.344074640000
N	33.651432927000	19.855524697495	3.884693256000
N	25.126199664500	1.036993449991	3.019693788000
N	27.064836369000	0.971572386703	1.636138620000
N	26.881339596500	7.273801483447	2.693090412000
N	-0.062147812000	30.171637613420	3.538041372000
N	-2.156957682000	31.325089835647	3.593677716000
N	-0.131528343500	32.543963121162	3.241267956000
N	-14.278727685500	25.135143698589	4.351844304000
N	-13.012733894500	23.186431175116	4.879348992000
N	-8.261372940000	27.452719664004	4.020246144000
N	-1.691116970500	46.118137784664	3.034608768000
N	0.245644584500	46.057820492271	1.648556208000
N	-0.411193497500	39.775542499933	2.826284652000
C	26.683913142000	14.756393594409	3.202350264000
C	26.779813645000	16.982565662890	3.344007888000
C	24.800727287000	15.961811483928	3.134712564000
C	28.685501294000	18.570302390348	3.570784956000
C	28.802564198500	19.958992052908	3.705366636000
C	29.818091592000	17.744419463733	3.549071520000
C	30.056235578500	20.530614393127	3.830999328000
C	31.075245392500	18.341560658426	3.665408364000
C	31.216149483500	19.734426133536	3.811158936000
C	32.496072956500	20.418331433441	3.956354532000
C	22.559387877500	16.973750058617	3.056738436000
C	21.236335966000	16.545497282625	2.864855484000
C	22.854054227500	18.325785366569	3.261455208000
C	20.202860713000	17.463248085346	2.888788824000

C	21.796202031000	19.237504440051	3.285180432000
C	20.466185278500	18.830594705983	3.107171880000
C	19.372705241500	19.794743425930	3.177792576000
C	26.891518979500	12.308903460762	3.083793516000
C	25.562573741000	11.897353934971	3.234608244000
C	27.909725158000	11.373985428667	2.845570068000
C	25.275407989000	10.533255168541	3.135406284000
C	27.607558210000	10.026589912438	2.760034392000
C	26.278880850000	9.580241948728	2.905368732000
C	25.955283622000	8.157681806593	2.816850060000
C	13.510720026000	22.670950314740	3.007137456000
C	11.291882410500	24.014170018420	3.030723936000
C	10.037407395000	24.767208214990	3.124168020000
C	8.803826902500	24.086550769291	3.171549096000
C	10.040889815500	26.172601127751	3.191736348000
C	7.612571213000	24.788551256914	3.270959172000
C	8.847223219500	26.875993552891	3.288649032000
C	7.609356671000	26.196264065536	3.305853288000
C	14.752872630500	21.895641117902	3.064438728000
C	14.726084780500	20.588147810486	3.588474816000
C	15.962879815000	22.403698311521	2.555178876000
C	15.867782947500	19.805878926064	3.579664572000
C	17.111007066000	21.618645552065	2.549837232000
C	17.079665281500	20.304192557066	3.063606264000
C	38.310375799000	23.069972402880	4.469291100000
C	37.112691025500	22.241769580404	4.294959264000
C	36.006888577500	22.733587502995	3.577583412000
C	37.053221998500	20.937988106367	4.826626272000
C	34.868404952500	21.954102493606	3.413657376000
C	35.913131102500	20.161286972011	4.668596856000
C	34.789648673500	20.665168353081	3.985698888000
C	26.178426412500	1.643878207301	2.415116808000
C	26.315848083000	3.101236787355	2.502664272000
C	25.429706005000	3.878865880055	3.273664680000
C	27.367806952500	3.745703857617	1.820598768000
C	25.577574937000	5.260595855031	3.347268372000
C	27.523444361000	5.119546186665	1.905579468000
C	26.622301087000	5.906454862810	2.650357260000
C	-1.403415461500	30.234274801675	3.664922760000
C	0.499861281000	31.356640419360	3.332422764000
C	-1.448151171000	32.449775349194	3.370161132000
C	2.801473353000	30.494567117310	3.097043568000

C	3.955493931000	30.935347330953	2.440576332000
C	2.732092821500	29.208880830990	3.651880824000
C	5.048438211000	30.088121362414	2.333119104000
C	3.847003138500	28.377430154309	3.550250844000
C	5.018971576000	28.800115180233	2.897529696000
C	6.219067256000	27.977016128652	2.792292372000
C	-3.286333438000	28.685048345514	4.050769824000
C	-4.392671643000	29.413495645955	3.588405444000
C	-3.452418108000	27.440656205525	4.667764392000
C	-5.665630275000	28.865072264349	3.741231960000
C	-4.728591282000	26.917287699221	4.823782020000
C	-5.857431281000	27.613256457604	4.353370488000
C	-7.165481996500	26.981780804165	4.503838356000
C	-13.097115622000	24.489748669981	4.504323960000
C	-11.852016354000	25.252530429169	4.368354840000
C	-10.637455235000	24.580688587743	4.135750524000
C	-11.844247877500	26.658851300275	4.453266168000
C	-9.450753480000	25.290576721294	4.007759184000
C	-10.656474608500	27.367811475481	4.333738212000
C	-9.434412891500	26.696897592400	4.133946852000
C	-1.879435556000	34.863395003266	3.070474092000
C	-0.622281755500	35.440121114380	3.304465848000
C	-2.966486509000	35.649375721067	2.673250020000
C	-0.479234636500	36.819067214322	3.148586964000
C	-2.804152138000	37.018114279220	2.518689204000
C	-1.561463776500	37.630102807425	2.761907436000
C	-1.475206899500	39.081429658240	2.623302180000
C	-0.670499885500	45.447223901583	2.443420584000
C	-0.610227223000	43.987081446495	2.566347768000
C	0.457000721000	43.266985771155	1.989935820000
C	-1.604592215000	43.278121271289	3.265201296000
C	0.523970346000	41.885255796179	2.101347252000
C	-1.551284393500	41.892215483762	3.356147988000
C	-0.496110982000	41.169799912561	2.757814488000
O	27.393255410000	13.613148913972	3.181885524000
O	27.352269999500	18.194015281649	3.466033236000
O	23.458388123500	15.905670004085	3.032666352000
O	-1.938100947500	29.019577328710	3.899885724000
O	1.830949547500	31.495370191865	3.176751996000
O	-2.247500615000	33.528990903860	3.259165932000
H	27.894456083500	20.560309060151	3.710430792000
H	29.709868678000	16.667987784101	3.448898352000

H	30.148921539500	21.612613822826	3.940745832000
H	31.973977760000	17.723076421809	3.653545752000
H	21.049088894500	15.483448957333	2.708213508000
H	23.878421611500	18.652426703837	3.399366744000
H	19.169117581500	17.148206227385	2.752958448000
H	22.017469672000	20.294448994449	3.451811976000
H	24.773135801500	12.618841547828	3.409286940000
H	28.932217392500	11.733569287165	2.733395544000
H	24.238450315500	10.206149852101	3.247233948000
H	28.386548888000	9.287935070207	2.575296756000
H	19.648084339500	20.844264313571	3.396869352000
H	24.880555080000	7.892285720063	2.840991516000
H	32.409548201000	21.503578717346	4.158435168000
H	8.802755388500	22.998055631180	3.129995268000
H	10.994269397000	26.701073404950	3.178208808000
H	6.657316482000	24.265182750610	3.307240728000
H	8.867314107000	27.962168795140	3.385145484000
H	13.788242152000	20.193301534897	3.976056180000
H	15.980559796000	23.410533115315	2.137628808000
H	15.853585387000	18.785588726274	3.963222360000
H	18.029026685500	22.003284285865	2.102457204000
H	36.056446100000	23.732534660861	3.143661552000
H	37.912844105000	20.550565497533	5.371265844000
H	34.036642210000	22.331317560649	2.817196920000
H	35.857412374500	19.158164001595	5.090517360000
H	24.625802626500	3.381016228225	3.816361836000
H	28.063487417000	3.145778787891	1.236625272000
H	24.900913846000	5.843353695384	3.974391252000
H	28.345831356000	5.623427567735	1.397984544000
H	3.973441790500	31.944502030608	2.031073416000
H	1.822645314000	28.867856139383	4.137901056000
H	5.950385120500	30.431001970711	1.821708720000
H	3.819947410000	27.374771163065	3.978067968000
H	7.011183980500	28.387637696098	2.137281948000
H	-4.257393000500	30.389243845208	3.131937684000
H	-2.569490572000	26.899656490676	5.004218592000
H	-6.539985699000	29.410711770921	3.382925580000
H	-4.856905083500	25.943395416657	5.300159544000
H	-7.158249277000	26.034799313592	5.077406052000
H	-10.641473412500	23.494513345494	4.043138904000
H	-12.785037169500	27.182219806579	4.623643800000
H	-8.526572655000	24.758856589889	3.775571100000

H	-10.645491590000	28.454914676075	4.412336688000
H	0.222339155000	34.822564836108	3.594163320000
H	-3.928706081000	35.166837381921	2.505855384000
H	0.487538870000	37.290006074162	3.332492136000
H	-3.655470011000	37.631494744942	2.216019168000
H	-2.417335584000	39.573711560002	2.315290500000
H	1.232241100000	43.814481194416	1.455216444000
H	-2.421353761500	43.831648423790	3.728259396000
H	1.353590060500	41.329872726989	1.663193700000
H	-2.316613268000	41.354463623118	3.917506212000

S14. Comparison study of MB adsorption on different adsorbents

Table S9: Comparison of the maximum equilibrium adsorption capacity of the MB dye on different adsorbents at room temperature.

Porous adsorbents	**SBET (m^2 /g)**	**Nature**	**Adsorption capacity (mg/g)**	**Ref.**
			MB	
TzTPT-COF	131	Amorphous	398.434	This work
Raw zeolite	24.59	Semi-crystalline	6.1	[8]
Raw kaolin	9.65	nm	13.99	[9]
Graphene oxide	24.92	nm	193.902	[10]
Magnetic multi-wall carbon nanotube	61.74	Crystalline	15.87	[11]
MOF-235	nm	Crystalline	187	[3]
1:1 Cu-Z-GO-M	46.696	Crystalline	94.481	[12]
Fe-BDC MOF	46.02	Crystalline	8.65	[13]
Pine leaves	nm	nm	126.58	[14]

Citric Acid Modified Sawdust	nm	Semi-crystalline	111.46	[15]
Turmeric powder	106.12	nm	157.33	[16]
Montmorillonite	22	Crystalline	556	[17]
Natural zeolite	nm	nm	19.94	[18]
Fly ash	6.52	nm	5.72	[19]
Modified Ball clay	92	nm	100	[20]
Activated carbon	1688	nm	270.3	[21]
Natural clay	128	Crystalline	62.5	[22]
carbon/montmorillonite nanocomposites	41.8	Crystalline	138.1	[23]
Kaolin	61.13	nm	45.0	[24]
Carbon nanotubes	160	nm	64.7	[25]
Rice husk	nm	nm	40.58	[26]
Rhassoul-clay	nm	nm	166	[27]
NaOH-treated raw kaolin	nm	nm	16.34	[9]
MIL-101(Cr)	1144	Crystalline	22	[28]
Fe_3O_4@MIL-100(Fe)	366.14	Crystalline	49	[29]

Zn-MOF	nm	Crystalline	.75	[30]
MWCNT	217	nm	45.2	[31]
MWCNTs/Fe_2O_3	114	Crystalline	42.3	[32]
$H_6P_2W_{18}O_{62}$/MOF-5	395	Crystalline	33.3	[33]
UiO-66–2.7Ti	929	Crystalline	33.3	[34]
UiO-66	1358	Crystalline	283	[34]
MIL101-Cr/PANI/Ag	2861	Crystalline	43.29	[35]
$Co_{0.3}Ni_{0.7}Fe_2O_4$@SiO_2 membrane	32.4	Crystalline	107.5	[36]
Graphene nanosheet	nm	Amorphous	111.6	[37]
Ultrathin-shell BN hollow sphere	215	Crystalline	191.7	[38]
Hollow octahedral carbon cage	1711	Crystalline	198.9	[39]
Hierarchical WO_3 hydrate	78.4	Crystalline	247.3	[40]
Well-defined microporous carbon	2264	microcrystalline	292	[41]
Polymer organic framework	3270	nm	351	[42]
Graphene oxide–chitosan hydrogel	nm	Crystalline	390	[43]
Activated carbon nanotube	729.3	Crystalline	399	[44]

TpPa-COOH covalent triazine framework	183	Crystalline	410	[45]
PUS-MOP-A porous polymer composite	306	Amorphous	240	[46]
CMP-YA conjugated microporous polymer	1410	Amorphous	1016	[47]
TPP-NH2 porous organic polymer	863	Amorphous	205	[48]
CalP covalent calix[4]arene polymer	596	Amorphous	625	[49]
THPP silsesquioxane porous polymer	915	Amorphous	862	[50]
TTMP microporous organic polymer	822	Amorphous	198	[51]
Fe-BC inorganic mesoporous biochar	217	Crystalline	156	[52]
HMONs-COOH microporous organic polymer	484	nm	198	[53]
Holey graphene nanosheets (Carbonaceous adsorbents)	1053	nm	269	[54]
NPCNS-10 (Carbonaceous adsorbents)	1120	Amorphous	962	[55]
Ordered mesoporous carbon (Carbonaceous adsorbents)	2580	Amorphous	758	[56]
Porous Carbon sheets (Carbonaceous adsorbents)	2315	Amorphous	769	[57]
ZJU-24 (Metal-organic-framework-based adsorbents)	1189	nm	902	[58]
BIT-1 (Metal-organic-framework-based adsorbents)	nm	nm	810	[59]
Amino-MIL-101(Al) (Metal-organic-framework-based adsorbents)	1980	Crystalline	762	[60]

THPS (Porous-organic-polymer-based adsorbents)	1426	Amorphous	330	61

nm- not mentioned

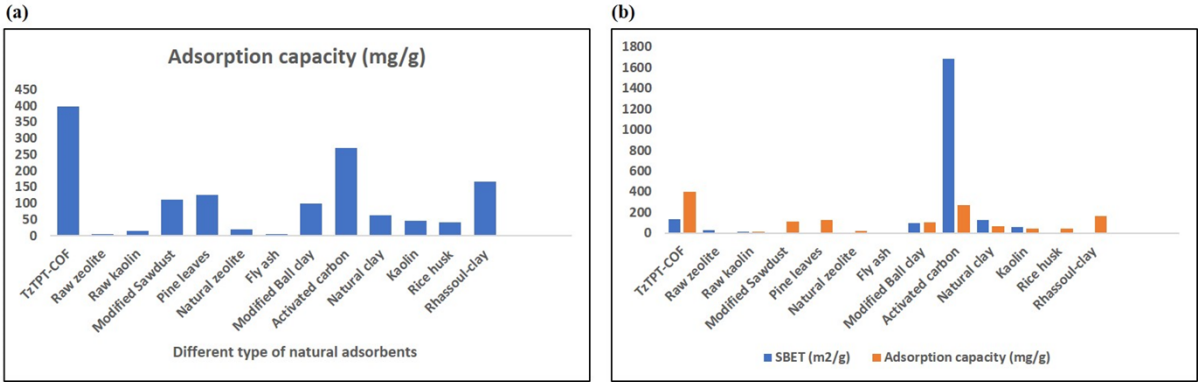

Figure S26. (a) Comparison of the adsorption capacity of TzTPT-COF with different type of natural adsorbents, (b) Comparison of the adsorption capacity and Bet Surface area of TzTPT-COF with different type of natural adsorbents.

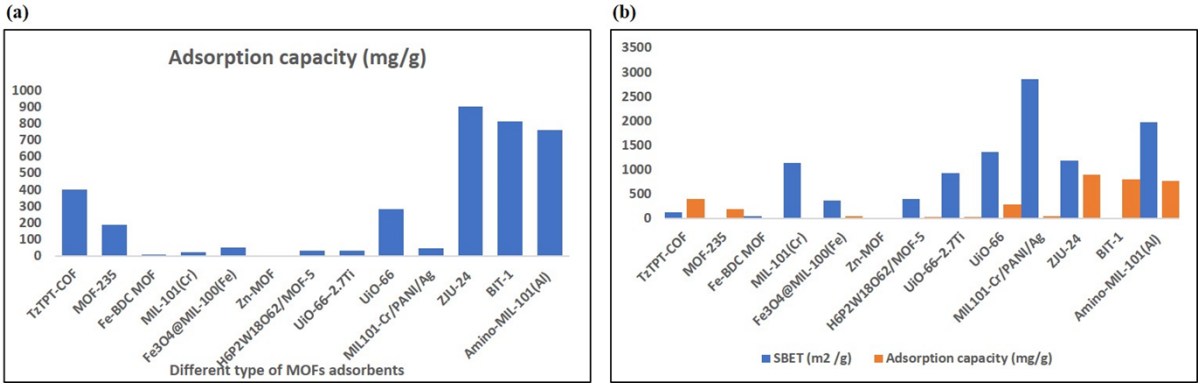

Figure S27. (a) Comparison of the adsorption capacity of TzTPT-COF with different type of MOFs adsorbents, (b) Comparison of the adsorption capacity and Bet Surface area of TzTPT-COF with different type of MOFs adsorbents.

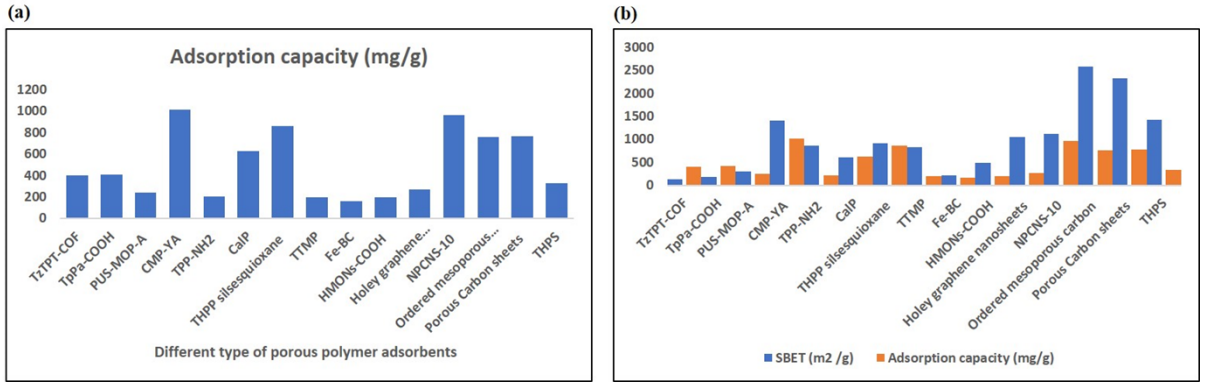

Figure S28. (a) Comparison of the adsorption capacity of TzTPT-COF with different type of porous polymer adsorbents, (b) Comparison of the adsorption capacity and Bet Surface area of TzTPT-COF with different type of porous polymer adsorbents.

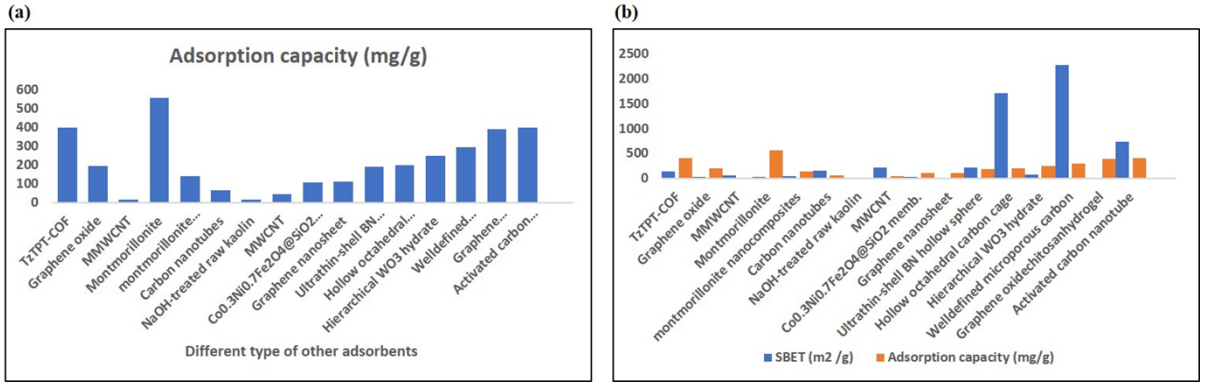

Figure S29. (a) Comparison of the adsorption capacity of TzTPT-COF with different type of other adsorbents, (b) Comparison of the adsorption capacity and Bet Surface area of TzTPT-COF with different type of other adsorbents.

References

1. R.-L. Wang, D.-P. Li, L.-J. Wang, X. Zhang, Z.-Y. Zhou, J.-L. Mu and Z.-M. Su, The preparation of new covalent organic framework embedded with silver nanoparticles and its applications in degradation of organic pollutants from waste water, *Dalton Transactions*, 2019, **48**, 1051-1059.
2. S. Haldar, D. Kaleeswaran, D. Rase, K. Roy, S. Ogale and R. Vaidhyanathan, Tuning the electronic energy level of covalent organic frameworks for crafting high-rate Na-ion battery anode, *Nanoscale Horizons*, 2020, **5**, 1264-1273.
3. E. Haque, J. W. Jun and S. H. Jhung, Adsorptive removal of methyl orange and methylene blue from aqueous solution with a metal-organic framework material, iron terephthalate (MOF-235), *Journal of Hazardous Materials*, 2011, **185**, 507-511.
4. T. Xu, S. An, C. Peng, J. Hu and H. Liu, Construction of Large-Pore Crystalline Covalent Organic Framework as High-Performance Adsorbent for Rhodamine B Dye Removal, *Industrial & Engineering Chemistry Research*, 2020, **59**, 8315-8322.

5. Y. Hou, J. Sun, D. Zhang, D. Qi and J. Jiang, Porphyrin–Alkaline Earth MOFs with the Highest Adsorption Capacity for Methylene Blue, *Chemistry – A European Journal*, 2016, **22**, 6345-6352.
6. L. Li, X. L. Liu, H. Y. Geng, B. Hu, G. W. Song and Z. S. Xu, A MOF/graphite oxide hybrid (MOF: HKUST-1) material for the adsorption of methylene blue from aqueous solution, *Journal of Materials Chemistry A*, 2013, **1**, 10292-10299.
7. S. Grimme, S. Ehrlich and L. Goerigk, Effect of the damping function in dispersion corrected density functional theory, *Journal of Computational Chemistry*, 2011, **32**, 1456-1465.
8. X. Jin, M.-q. Jiang, X.-q. Shan, Z.-g. Pei and Z. Chen, Adsorption of methylene blue and orange II onto unmodified and surfactant-modified zeolite, *Journal of Colloid and Interface Science*, 2008, **328**, 243-247.
9. D. Ghosh and K. G. Bhattacharyya, Adsorption of methylene blue on kaolinite, *Applied Clay Science*, 2002, **20**, 295-300.
10. K. He, G. Chen, G. Zeng, A. Chen, Z. Huang, J. Shi, M. Peng, T. Huang and L. Hu, Enhanced removal performance for methylene blue by kaolin with graphene oxide modification, *Journal of the Taiwan Institute of Chemical Engineers*, 2018, **89**, 77-85.
11. J.-L. Gong, B. Wang, G.-M. Zeng, C.-P. Yang, C.-G. Niu, Q.-Y. Niu, W.-J. Zhou and Y. Liang, Removal of cationic dyes from aqueous solution using magnetic multi-wall carbon nanotube nanocomposite as adsorbent, *Journal of Hazardous Materials*, 2009, **164**, 1517-1522.
12. T. Huang, M. Yan, K. He, Z. Huang, G. Zeng, A. Chen, M. Peng, H. Li, L. Yuan and G. Chen, Efficient removal of methylene blue from aqueous solutions using magnetic graphene oxide modified zeolite, *Journal of Colloid and Interface Science*, 2019, **543**, 43-51.
13. C. Arora, S. Soni, S. Sahu, J. Mittal, P. Kumar and P. K. Bajpai, Iron based metal organic framework for efficient removal of methylene blue dye from industrial waste, *Journal of Molecular Liquids*, 2019, **284**, 343-352.
14. M. T. Yagub, T. K. Sen and H. M. Ang, Equilibrium, Kinetics, and Thermodynamics of Methylene Blue Adsorption by Pine Tree Leaves, *Water, Air, & Soil Pollution*, 2012, **223**, 5267-5282.
15. W. Zou, H. Bai, S. Gao and K. Li, Characterization of modified sawdust, kinetic and equilibrium study about methylene blue adsorption in batch mode, *Korean Journal of Chemical Engineering*, 2013, **30**, 111-122.
16. K. T. Kubra, M. S. Salman and M. N. Hasan, Enhanced toxic dye removal from wastewater using biodegradable polymeric natural adsorbent, *Journal of Molecular Liquids*, 2021, **328**, 115468.
17. F. G. E. Nogueira, J. H. Lopes, A. C. Silva, M. Gonçalves, A. S. Anastácio, K. Sapag and L. C. A. Oliveira, Reactive adsorption of methylene blue on montmorillonite via an ESI-MS study, *Applied Clay Science*, 2009, **43**, 190-195.
18. R. Han, J. Zhang, P. Han, Y. Wang, Z. Zhao and M. Tang, Study of equilibrium, kinetic and thermodynamic parameters about methylene blue adsorption onto natural zeolite, *Chemical Engineering Journal*, 2009, **145**, 496-504.
19. K. V. Kumar, V. Ramamurthi and S. Sivanesan, Modeling the mechanism involved during the sorption of methylene blue onto fly ash, *Journal of Colloid and Interface Science*, 2005, **284**, 14-21.
20. M. Auta and B. H. Hameed, Modified mesoporous clay adsorbent for adsorption isotherm and kinetics of methylene blue, *Chemical Engineering Journal*, 2012, **198-199**, 219-227.
21. Y. Li, Q. Du, T. Liu, X. Peng, J. Wang, J. Sun, Y. Wang, S. Wu, Z. Wang, Y. Xia and L. Xia, Comparative study of methylene blue dye adsorption onto activated carbon, graphene oxide, and carbon nanotubes, *Chemical Engineering Research and Design*, 2013, **91**, 361-368.
22. O. Sakin Omer, M. A. Hussein, B. H. M. Hussein and A. Mgaidi, Adsorption thermodynamics of cationic dyes (methylene blue and crystal violet) to a natural clay mineral from aqueous solution between 293.15 and 323.15 K, *Arabian Journal of Chemistry*, 2018, **11**, 615-623.

23. D. S. Tong, C. W. Wu, M. O. Adebajo, G. C. Jin, W. H. Yu, S. F. Ji and C. H. Zhou, Adsorption of methylene blue from aqueous solution onto porous cellulose-derived carbon/montmorillonite nanocomposites, *Applied Clay Science*, 2018, **161**, 256-264.
24. K. Rida, S. Bouraoui and S. Hadnine, Adsorption of methylene blue from aqueous solution by kaolin and zeolite, *Applied Clay Science*, 2013, **83-84**, 99-105.
25. Y. Yao, F. Xu, M. Chen, Z. Xu and Z. Zhu, Adsorption behavior of methylene blue on carbon nanotubes, *Bioresource Technology*, 2010, **101**, 3040-3046.
26. V. Vadivelan and K. V. Kumar, Equilibrium, kinetics, mechanism, and process design for the sorption of methylene blue onto rice husk, *Journal of Colloid and Interface Science*, 2005, **286**, 90-100.
27. Y. Bentahar, K. Draoui, C. Hurel, O. Ajouyed, S. Khairoun and N. Marmier, Physico-chemical characterization and valorization of swelling and non-swelling Moroccan clays in basic dye removal from aqueous solutions, *Journal of African Earth Sciences*, 2019, **154**, 80-88.
28. T. Shen, J. Luo, S. Zhang and X. Luo, Hierarchically mesostructured MIL-101 metal–organic frameworks with different mineralizing agents for adsorptive removal of methyl orange and methylene blue from aqueous solution, *Journal of Environmental Chemical Engineering*, 2015, **3**, 1372-1383.
29. Y. Shao, L. Zhou, C. Bao, J. Ma, M. Liu and F. Wang, Magnetic responsive metal–organic frameworks nanosphere with core–shell structure for highly efficient removal of methylene blue, *Chemical Engineering Journal*, 2016, **283**, 1127-1136.
30. C.-Y. Sun, X.-L. Wang, C. Qin, J.-L. Jin, Z.-M. Su, P. Huang and K.-Z. Shao, Solvatochromic Behavior of Chiral Mesoporous Metal–Organic Frameworks and Their Applications for Sensing Small Molecules and Separating Cationic Dyes, *Chemistry – A European Journal*, 2013, **19**, 3639-3645.
31. S. Wang, C. W. Ng, W. Wang, Q. Li and Z. Hao, Synergistic and competitive adsorption of organic dyes on multiwalled carbon nanotubes, *Chemical Engineering Journal*, 2012, **197**, 34-40.
32. S. Qu, F. Huang, S. Yu, G. Chen and J. Kong, Magnetic removal of dyes from aqueous solution using multi-walled carbon nanotubes filled with Fe2O3 particles, *Journal of Hazardous Materials*, 2008, **160**, 643-647.
33. X. Liu, W. Gong, J. Luo, C. Zou, Y. Yang and S. Yang, Selective adsorption of cationic dyes from aqueous solution by polyoxometalate-based metal–organic framework composite, *Applied Surface Science*, 2016, **362**, 517-524.
34. Y. Han, M. Liu, K. Li, Q. Sun, W. Zhang, C. Song, G. Zhang, Z. Conrad Zhang and X. Guo, In situ synthesis of titanium doped hybrid metal–organic framework UiO-66 with enhanced adsorption capacity for organic dyes, *Inorganic Chemistry Frontiers*, 2017, **4**, 1870-1880.
35. K. Karami, S. M. Beram, P. Bayat, F. Siadatnasab and A. Ramezanpour, A novel nanohybrid based on metal–organic framework MIL101−Cr/PANI/Ag for the adsorption of cationic methylene blue dye from aqueous solution, *Journal of Molecular Structure*, 2022, **1247**, 131352.
36. Z. Zhu, G. Li, G. Zeng, X. Chen, D. Hu, Y. Zhang and Y. Sun, Fast capture of methyl-dyes over hierarchical amino-Co0.3Ni0.7Fe2O4@SiO2 nanofibrous membranes, *Journal of Materials Chemistry A*, 2015, **3**, 22000-22004.
37. Z.-J. Fan, W. Kai, J. Yan, T. Wei, L.-J. Zhi, J. Feng, Y.-m. Ren, L.-P. Song and F. Wei, Facile Synthesis of Graphene Nanosheets via Fe Reduction of Exfoliated Graphite Oxide, *ACS Nano*, 2011, **5**, 191-198.
38. G. Lian, X. Zhang, S. Zhang, D. Liu, D. Cui and Q. Wang, Controlled fabrication of ultrathin-shell BN hollow spheres with excellent performance in hydrogen storage and wastewater treatment, *Energy & Environmental Science*, 2012, **5**, 7072-7080.

39. A. Aijaz, J.-K. Sun, P. Pachfule, T. Uchida and Q. Xu, From a metal–organic framework to hierarchical high surface-area hollow octahedral carbon cages, *Chemical Communications*, 2015, **51**, 13945-13948.
40. B. Liu, J. Wang, J. Wu, H. Li, Z. Li, M. Zhou and T. Zuo, Controlled fabrication of hierarchical WO3 hydrates with excellent adsorption performance, *Journal of Materials Chemistry A*, 2014, **2**, 1947-1954.
41. Z. Li, D. Wu, Y. Liang, R. Fu and K. Matyjaszewski, Synthesis of Well-Defined Microporous Carbons by Molecular-Scale Templating with Polyhedral Oligomeric Silsesquioxane Moieties, *Journal of the American Chemical Society*, 2014, **136**, 4805-4808.
42. P. Kuhn, K. Krüger, A. Thomas and M. Antonietti, "Everything is surface": tunable polymer organic frameworks with ultrahigh dye sorption capacity, *Chemical Communications*, 2008, DOI: 10.1039/B814254H, 5815-5817.
43. Y. Chen, L. Chen, H. Bai and L. Li, Graphene oxide–chitosan composite hydrogels as broad-spectrum adsorbents for water purification, *Journal of Materials Chemistry A*, 2013, **1**, 1992-2001.
44. J. Ma, F. Yu, L. Zhou, L. Jin, M. Yang, J. Luan, Y. Tang, H. Fan, Z. Yuan and J. Chen, Enhanced Adsorptive Removal of Methyl Orange and Methylene Blue from Aqueous Solution by Alkali-Activated Multiwalled Carbon Nanotubes, *ACS Applied Materials & Interfaces*, 2012, **4**, 5749-5760.
45. B. Dong, W.-J. Wang, S.-C. Xi, D.-Y. Wang and R. Wang, A Carboxyl-Functionalized Covalent Organic Framework Synthesized in a Deep Eutectic Solvent for Dye Adsorption, *Chemistry – A European Journal*, 2021, **27**, 2692-2698.
46. T. J. Choi, D. Y. Kim and J. Y. Chang, Water wettable, compressible, and hierarchically porous polymer composite, *Microporous and Mesoporous Materials*, 2017, **242**, 82-89.
47. Y. Yuan, H. Huang, L. Chen and Y. Chen, N,N'-Bicarbazole: A Versatile Building Block toward the Construction of Conjugated Porous Polymers for CO2 Capture and Dyes Adsorption, *Macromolecules*, 2017, **50**, 4993-5003.
48. Y. He, T. Xu, J. Hu, C. Peng, Q. Yang, H. Wang and H. Liu, Amine functionalized 3D porous organic polymer as an effective adsorbent for removing organic dyes and solvents, *RSC Advances*, 2017, **7**, 30500-30505.
49. D. Shetty, I. Jahovic, J. Raya, F. Ravaux, M. Jouiad, J.-C. Olsen and A. Trabolsi, An ultra-absorbent alkyne-rich porous covalent polycalix[4]arene for water purification, *Journal of Materials Chemistry A*, 2017, **5**, 62-66.
50. M. Ge and H. Liu, A silsesquioxane-based thiophene-bridged hybrid nanoporous network as a highly efficient adsorbent for wastewater treatment, *Journal of Materials Chemistry A*, 2016, **4**, 16714-16722.
51. R. Bera, M. Ansari, S. Mondal and N. Das, Selective CO2 capture and versatile dye adsorption using a microporous polymer with triptycene and 1,2,3-triazole motifs, *European Polymer Journal*, 2018, **99**, 259-267.
52. R. Lin, Z. Liang, C. Yang, Z. Zhao and F. Cui, Selective adsorption of organic pigments on inorganically modified mesoporous biochar and its mechanism based on molecular structure, *Journal of Colloid and Interface Science*, 2020, **573**, 21-30.
53. M. Zhou, Z. He, T. Wang, Y. Xu, W. Yu, B. Shi and K. Huang, Carboxyl group functionalized hollow microporous organic nanospheres for efficient catalysis and adsorption, *Microporous and Mesoporous Materials*, 2019, **274**, 245-250.
54. Z. Xing, J. Tian, Q. Liu, A. M. Asiri, P. Jiang and X. Sun, Holey graphene nanosheets: large-scale rapid preparation and their application toward highly-effective water cleaning, *Nanoscale*, 2014, **6**, 11659-11663.
55. J. Gong, H. Lin, M. Antonietti and J. Yuan, Nitrogen-doped porous carbon nanosheets derived from poly(ionic liquid)s: hierarchical pore structures for efficient CO2 capture and dye removal, *Journal of Materials Chemistry A*, 2016, **4**, 7313-7321.

56. X. Zhuang, Y. Wan, C. Feng, Y. Shen and D. Zhao, Highly Efficient Adsorption of Bulky Dye Molecules in Wastewater on Ordered Mesoporous Carbons, *Chemistry of Materials*, 2009, **21**, 706-716.
57. J. Gong, J. Liu, X. Chen, Z. Jiang, X. Wen, E. Mijowska and T. Tang, Converting real-world mixed waste plastics into porous carbon nanosheets with excellent performance in the adsorption of an organic dye from wastewater, *Journal of Materials Chemistry A*, 2015, **3**, 341-351.
58. Q. Zhang, J. Yu, J. Cai, R. Song, Y. Cui, Y. Yang, B. Chen and G. Qian, A porous metal–organic framework with –COOH groups for highly efficient pollutant removal, *Chemical Communications*, 2014, **50**, 14455-14458.
59. R. Li, X. Ren, J. Zhao, X. Feng, X. Jiang, X. Fan, Z. Lin, X. Li, C. Hu and B. Wang, Polyoxometallates trapped in a zeolitic imidazolate framework leading to high uptake and selectivity of bioactive molecules, *Journal of Materials Chemistry A*, 2014, **2**, 2168-2173.
60. E. Haque, V. Lo, A. I. Minett, A. T. Harris and T. L. Church, Dichotomous adsorption behaviour of dyes on an amino-functionalised metal–organic framework, amino-MIL-101(Al), *Journal of Materials Chemistry A*, 2014, **2**, 193-203.
61. C. Zhang, P.-C. Zhu, L. Tan, J.-M. Liu, B. Tan, X.-L. Yang and H.-B. Xu, Triptycene-Based Hyper-Cross-Linked Polymer Sponge for Gas Storage and Water Treatment, *Macromolecules*, 2015, **48**, 8509-8514.